

Mycobacterium tuberculosis FtsB and PerM interact via a C-terminal helix in FtsB to modulate cell division

João Ramalheira Ferreira^{1†}, Ruilan Xu^{1†}, Zach Hensel^{1*}

¹ITQB NOVA, Universidade NOVA de Lisboa, Av. da República, Oeiras, 2780-157, Portugal.

*Corresponding author(s). E-mail(s): zach.hensel@itqb.unl.pt;

†These authors contributed equally to this work.

Abstract

Latent infection by *Mycobacterium tuberculosis* (Mtb) impedes effective tuberculosis therapy and eradication. The protein PerM is essential for chronic Mtb infections in mice and acts via the divisome protein FtsB to modulate cell division. Using transgenic co-expression in *Escherichia coli*, we studied the Mtb PerM-FtsB interaction in isolation from other Mtb proteins, engineering PerM to enhance expression in the *E. coli* membrane. We confirmed the reported instability of Mtb FtsB, and we linked FtsB instability to a segment of FtsB predicted to bind cell-division proteins FtsL and FtsQ. Using fluorescence microscopy, we found that PerM stability hinged on its interaction with a C-terminal helix in FtsB. Molecular dynamics results supported the observation that FtsB stabilized PerM, and suggested that interactions at the PerM-FtsB interface differ from our initial structure prediction in a way that is consistent with PerM sequence conservation. Though narrowly conserved, the PerM-FtsB interaction emerges as a potential target for therapy targeting persistent infections by disrupting regulation of cell division. Integrating protein structure prediction, molecular dynamics and single-molecule microscopy, our approach is primed to screen potential inhibitors of the PerM-FtsB interaction and can be straightforwardly adapted to explore other putative interactions.

Keywords: *Mycobacterium tuberculosis*, cell division, single-molecule microscopy, molecular dynamics

1 Importance

2 Our research reveals significant insights into the dynamic interaction between the proteins PerM and FtsB
3 within *Mycobacterium tuberculosis*, contributing to our understanding of bacterial cell division mechanisms
4 crucial for infection persistence. By combining innovative fluorescence microscopy and molecular dynamics, we
5 established that the stability of these proteins is interdependent; molecular dynamics placing PerM-FtsB in
6 the context of the mycobacterial divisome show how disrupting PerM-FtsB interaction can plausibly impact
7 bacterial cell wall synthesis. These findings highlight the PerM-FtsB interface as a promising target for novel
8 therapeutics aimed at combating persistent bacterial infections. Importantly, our approach can be adapted for
9 similar studies in other bacterial systems, suggesting broad implications for microbial biology and antibiotic
10 development.

11 Introduction

12 *Mycobacterium tuberculosis* (Mtb) is a major contributor to preventable deaths by infectious disease and has
13 infected approximately a quarter of the global population [1]. Most infections progress to latent tuberculosis
14 infection (LTBI), characterized by an immunological response to Mtb antigens without clinical signs of active
15 TB [2]. Preventing establishment and reactivation of LTBI is a growing priority for TB elimination strategies,
16 although uncertainties continue to limit measurements of the relative burdens of new TB infections and LTBI

17 reactivation [3]. Protocols that reduce the duration and adverse effects of treatment can reduce LTBI burden by
18 improving completion rates for preventative treatment [4]. Furthermore, imperfect treatment over long periods
19 can contribute to acquisition of drug resistance [5]. Consequently, it is imperative to better understand how
20 Mtb infections persist to establish LTBI in order to inform strategies for novel LTBI treatments with higher
21 efficacy, shorter durations, and reduced risk of drug resistance.

22 A potential strategy to prevent establishment and reactivation of LTBI is to characterize and target mech-
23 anisms through which Mtb persists through host-induced stress [6]. The actinomycete protein PerM was one
24 of 21 genes identified in a screen of transposon Mtb mutants with attenuated growth at pH 4.5 in media
25 containing Tween 80, with most of the identified genes being associated with cell wall synthesis [7]. A subse-
26 quent study focused on PerM, finding that Mtb PerM knockout reduced growth during chronic mouse infection
27 and increased β -lactam antibiotic susceptibility. Localization of fluorescently tagged PerM to dividing septa
28 suggested a connection to cell division [8]. Further work demonstrated that PerM associates with the Mtb
29 divisome, a protein complex orchestrating cell wall remodeling during division, and that PerM depletion can
30 be complemented by overexpression of the divisome component FtsB [9]. PerM was also recently identified by
31 transposon sequencing to play an even more significant role in infecting mice in a background with weakened
32 adaptive immune response [10].

33 Recently, a covalent inhibitor of divisome formation based upon the structure of FtsB-FtsQ was developed
34 and found to be active against drug-resistant *E. coli* in an animal infection model [11]. The Mtb proteome
35 includes homologs of the five core *E. coli* divisome proteins FtsQ, FtsL, FtsB, FtsW, and FtsI [12], suggesting
36 that a similar approach can target protein-protein interactions in the Mtb divisome. However, it is unknown
37 whether PerM directly interacts with FtsB [9] and, if it does, whether PerM has a regulatory role beyond
38 impacting FtsB stability. PerM lacks known orthologs outside of actinomycetes [8], so PerM interactions could
39 potentially be targeted by specific therapies. However, no experimental structural data have been published
40 on the PerM-FtsB interaction or on PerM alone to guide experimental design. Expression and purification of
41 Mtb PerM and FtsB for structural study is likely to pose difficulties given that FtsB stability depends upon
42 PerM co-expression in Mtb and *Mycobacterium smegmatis* [9]. Furthermore, proteins such as PerM with a
43 high number of transmembrane helices pose challenges for recombinant expression [13, 14].

44 Recent insights into the molecular structure and regulatory mechanisms of the gram-negative divisome have
45 been enabled by the confluence of protein structure prediction, cryogenic electron microscopy (Cryo-EM), and
46 molecular dynamics (MD) simulations. The extension from prediction of monomers to protein complexes [15, 16]
47 facilitated rapid structure prediction of the core *E. coli* divisome [17, 18]. Analysis of a Cryo-EM structure
48 of the *Pseudomonas aeruginosa* divisome was largely consistent with predicted protein-protein interfaces, but
49 also revealed a global conformational change absent in structure predictions [19]. All-atom MD simulations
50 identified a similar conformational change within 1 μ s, and further predicted interactions between the core
51 divisome and *E. coli* FtsN [20]. However, limitations of this MD approach, such as uncertainty in structure
52 predictions and limited MD timescales, call for experimental validation. Importantly, *in silico* predictions for
53 FtsN were corroborated by experimental results in living cells [21].

54 In this work, we employed a combination of structure prediction, MD, and fluorescence microscopy to
55 probe the predicted interaction between Mtb PerM and FtsB proteins. In our approach, Mtb PerM and FtsB
56 were expressed *E. coli* in order to directly attribute observations to changes in the Mtb proteins. First, we
57 investigated conservation and dynamics at the predicted PerM-FtsB interface, identifying roles for conserved
58 residues that are absent in structure predictions. Second, we showed that FtsB instability (when expressed in
59 *E. coli*) depends on a region predicted to bind FtsL and FtsQ, and that PerM expression in the *E. coli* membrane
60 can be enhanced by strategically modifying its N-terminal signal sequence. This enabled the quantification of
61 the PerM-FtsB interaction via fluorescence correlation and single-molecule tracking. We found PerM expression
62 in the *E. coli* membrane to depend on the FtsB sequence predicted to mediate PerM-FtsB interaction. Lastly,
63 we investigated MD simulations of Mtb divisome complexes suggested PerM regulatory complexity beyond
64 FtsB stabilization.

65 Results

66 Structure prediction and molecular dynamics of PerM-FtsB interaction

67 In preliminary structure predictions, we identified a high-confidence predicted interaction between Mtb PerM
68 and FtsB ($pDockQ \approx 0.6$ [22]). The predicted structure of PerM was largely consistent with previous predicted
69 topology [8] except that two regions with hydrophobic residues in predicted transmembrane helices did not
70 span the membrane in structure predictions (Fig. 1A). The topology remains N-in, C-in, with the predicted

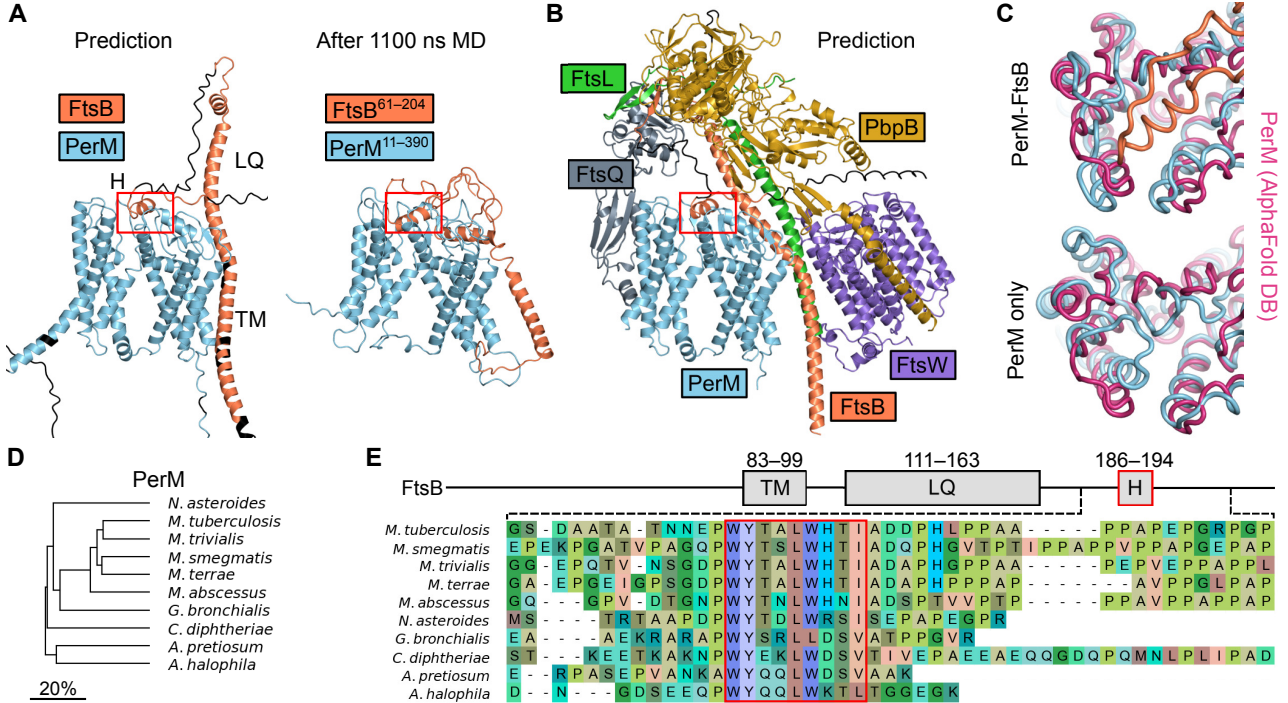


Fig. 1 A conserved, predicted Mtb PerM-FtsB interaction stabilizes PerM in MD. (A) Left: predicted PerM-FtsB complex in which an α helix, FtsB^H, interacts with the periplasmic face of PerM. Transmembrane helix FtsBTM and the region interacting with FtsL and FtsQ, FtsB^{LQ}, are indicated. Residues with $pLDLT < 50$ colored black. Right: final conformer following 1.1 μ s MD; PerM-FtsB^H interact persists, FtsB^{LQ} collapses, and FtsBTM moves away from PerM. (B) Prediction for the Mtb divisome with inclusion of PerM. Terminal regions with $pLDLT < 50$ are omitted except for the FtsB C-terminus. All complexes in A and B are aligned by PerM C α atoms; the red box is placed at the same position relative to PerM for comparison of FtsB^H movement. (C) Final MD conformers for PerM-FtsB and for PerM alone are aligned by PerM C α atoms and compared to a PerM prediction (AlphaFold DB P9WKN3-F1-model.v4). (D) Phylogenetic tree for actinomycete species with predicted PerM-FtsB interactions. Branch length scaled by divergence in amino acid identity in pairwise sequence alignments of PerM. (E) Top: Diagram of Mtb FtsB defining the FtsBTM, FtsB^{LQ}, and FtsB^H regions. Bottom: Multiple sequence alignment of a region near the C-terminus of FtsB for actinomycete species illustrates conservation of residues in FtsB^H and diversity in FtsB C-termini.

71 PerM structure consisting of two halves, each with the same topology (four transmembrane helices with a
 72 buried extracellular loop between the first two). Preliminary molecular dynamics (MD) simulations showed that
 73 the predicted PerM-FtsB interaction persisted on the microsecond timescale. To test stability of the structure
 74 of the predicted complex further, we carried out a three-stage MD protocol with 100 ns of equilibrium MD
 75 followed by 500 ns of accelerated molecular dynamics (aMD), and a final 500 ns of equilibrium MD. Terminal
 76 residues lacking high local prediction confidence ($pLDLT < 50$) were omitted in constructing the simulation
 77 system of FtsB^{61–204} and PerM^{11–390}. Fig. 1A shows how the predicted extended structure of FtsB collapsed
 78 in the absence of interactions with other divisome components [17–20]. Interaction between transmembrane
 79 helices of PerM and FtsB was not predicted with high confidence and also did not exhibit persistent, specific
 80 interactions in MD. Conversely, the predicted interaction between FtsB and a specific pocket in the periplasmic
 81 face of PerM was maintained throughout the aMD protocol and in a simulation replicate.

82 We also found that a prediction of the core Mtb divisome with the addition of PerM was consistent with
 83 PerM interacting with the divisome without obviously disrupting interactions between core divisome com-
 84 ponents (Fig. 1B). Within this complex, PerM was only predicted to interact with FtsB. Based on these
 85 predictions, we identified three regions of interest in Mtb FtsB: the predicted transmembrane helix, FtsBTM
 86 (FtsB^{83–99}), the region predicted to interact with FtsL and FtsQ, FtsB^{LQ} (FtsB^{111–163}), and a span of
 87 hydrophobic residues forming an α helix predicted to interact with PerM, FtsB^H (FtsB^{186–194}). Although C-
 88 terminal residues following FtsB^H were predicted to thread between the PpbB anchor and head domains, there
 89 were no high-confidence predictions for this region.

90 In order to see the impact of FtsB on PerM, we replicated the three-stage MD protocol using PerM alone.
 91 Final conformers for PerM-FtsB and PerM simulations are shown in Fig. 1C and compared to a PerM structure
 92 prediction from the AlphaFold Protein Structure Database [23]. Surprisingly, we found that the final conformer
 93 in the monomeric PerM simulation differed from the predicted PerM structure ($RMSD = 3.47 \text{ \AA}$) to a greater

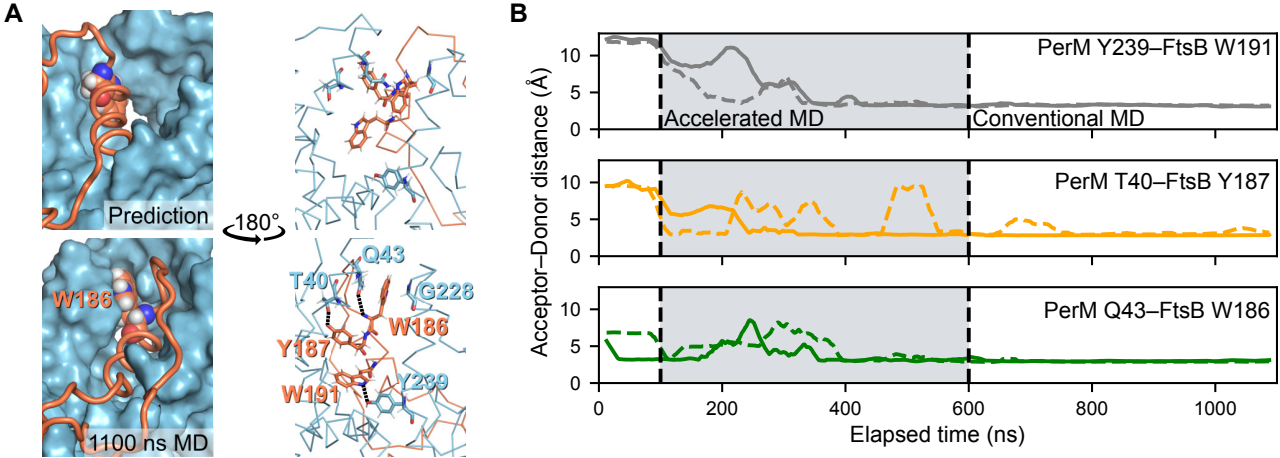


Fig. 2 Reproducible dynamics at the PerM-FtsB binding interface. (A) The shape of the FtsB binding pocket for PerM is compared between the predicted interface structure (top) and the final conformer following 1.1 μ s MD (bottom). Left: a large predicted periplasmic binding pocket in PerM (top left) changes to tightly bind FtsB W186 (bottom left). Right: Following MD (bottom right), FtsB W186 interacts with conserved PerM residue G228 and hydrogen bonds are formed between conserved FtsB residues and PerM residues including highly conserved Y239. The same region is shown rotated by 180°. (B) Interactions at the PerM-FtsB interface appeared in two independent aMD simulations. Solid and dashed lines show acceptor-donor distance (25 ns moving average; two MD replicates) for hydrogen bonds at the PerM-FtsB interface that are absent in the predicted structure.

94 extent than final conformers in PerM-FtsB simulation replicates (2.50 \AA and 2.21 \AA). The largest structural
95 changes were seen in the predicted FtsB^H binding pocket.

96 Since our structure predictions were informed by information encoded in multiple sequence alignments, we
97 searched for and identified PerM orthologs in actinomycete species (Fig. 1D). For each, we also identified the
98 corresponding FtsB sequence and predicted the structures of PerM-FtsB complexes. In every species tested
99 there was a predicted interaction between PerM and FtsB^H with the same orientation of FtsB^H on the periplasmic
100 face of PerM (Supplementary Fig. S1). Further, there is little difference in the lengths of regions linking
101 FtsB^{LQ} and FtsB^H. PerM-FtsB complexes differed, however, in the predicted position of FtsBTM relative to
102 PerM. We constructed a multiple sequence alignment of FtsB to investigate the basis for conserved, predicted
103 PerM-FtsB interaction and found that FtsB^H was highly conserved (Fig. 1E) with near perfect conservation
104 of hydrophobic residues predicted to interact with PerM (W186, Y187, L190, and W191).

105 Next, we investigated the structural basis for specific PerM-FtsB interaction. Fig. 2A illustrates how the
106 FtsB binding pocket of PerM changed during MD, focusing on hydrogen bonds formed during MD that were
107 not observed in structure predictions. These include a sidechain-sidechain hydrogen bond with PerM Y239,
108 which is perfectly conserved in PerM for the species shown in Fig. 1D. We observed that a large, hydrophobic
109 binding pocket tightened around FtsB^H, and around FtsB W186 in particular. Residues in the W186 binding
110 pocket include PerM G228, which was conserved in mycobacterial sequences in species that we analyzed.

111 Fig. 2B shows that hydrogen bonding interactions at the PerM-FtsB binding interface were reproduced in
112 a replicate simulation. However, we observed that the α -helical secondary structure of FtsB^H was partially
113 lost in the second simulation (Supplementary Fig. S2A). To further assess reproducibility, we conducted two
114 additional replicate aMD simulations (differing only in using shorter, 50 ns final steps) that also demonstrated
115 loss of α -helical dihedral angles in FtsB^H and, further, failed to reproduce the interactions shown in Fig. 2A
116 (Supplementary Fig. S2B). We suspected that a reduced dihedral boost in aMD would maintain secondary structure
117 while still more rapidly exploring conformations at the PerM-FtsB interface than conventional MD. Two
118 final simulations with reduced dihedral boost confirmed this hypothesis, maintaining α -helical dihedral angles
119 and more frequently exhibiting the hydrogen bonds observed in our full-length simulations (Supplementary
120 Fig. S2C).

121 Transgenic expression of fluorescent FtsB and PerM constructs in *E. coli*

122 Despite the apparent specificity and stability of the predicted PerM-FtsB interface in MD, we wanted to confirm
123 that this interaction does not depend on other Mtb components to be stable on timescales inaccessible by MD
124 and, if so, to investigate whether FtsB^H mediated the interaction. Rather than reconstitute a minimal system
125 *in vitro*, we aimed to investigate the bimolecular interaction in *E. coli* cells using Mtb FtsB and PerM fused

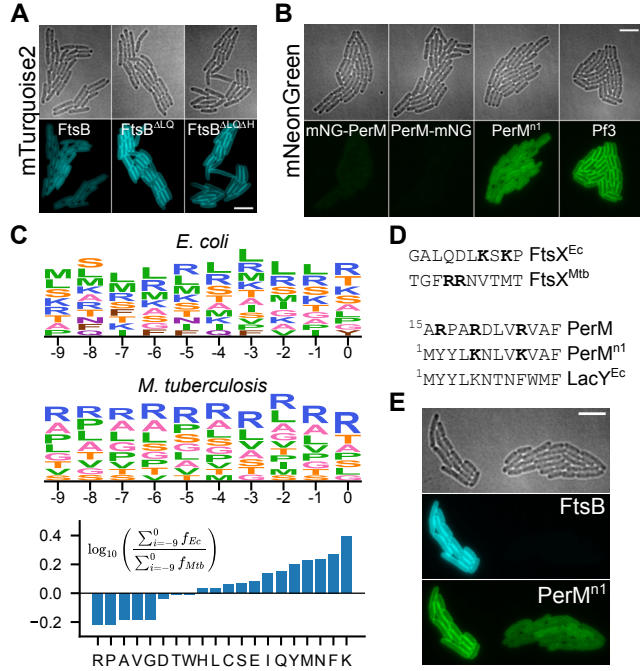


Fig. 3 Expression of fluorescent fusion proteins with Mtb FtsB and PerM in *E. coli*. (A) Expression and membrane localization of FtsB and variants with deletions of FtsB^{LQ} or with deletion of both FtsB^{LQ} and FtsB^H. Identical minimum and maximum intensities used to produce figures. (B) Expression and membrane localization for mNG-PerM, PerM-mNG, PerMⁿ¹-mNG, and Pf3-mNG. Identical minimum and maximum intensities used to produce figures. (C) Top: residue frequency for positions preceding the first predicted transmembrane helix, inclusive of residues found at frequencies above 5 %. Letter height is proportional to residue frequency with more frequent residues on top. Bottom: relative frequencies in *E. coli* and Mtb. (D) Top: residues preceding the first transmembrane helix in paralogs of FtsX, highlighting lysine and arginine residues. Bottom: comparison of PerM to PerMⁿ¹ and *E. coli* LacY. (E) Two adjacent microcolonies from a strain with co-expression of mTq2-FtsB and PerMⁿ¹-mNG. The microcolony on the right has coincidentally lost the plasmid encoding mTq2-FtsB, and exhibits reduced membrane localization of PerMⁿ¹-mNG. Scale bars 5 μm.

to fluorescent proteins. We chose the fluorescent proteins mNeonGreen [24] and mTurquoise2 [25] since these bright, fast-maturing fluorescent proteins can be spectrally separated with appropriate filter sets.

We constructed variants of FtsB with an N-terminal fusion of mTurquoise2 (mTq2-FtsB, mTq2-FtsB^{ΔLQ}, and mTq2-FtsB^{ΔLQΔH}; Fig. 3A). Deletion of the FtsB^{LQ} region was based upon the observation of hydrophobic interactions of Mtb FtsB with FtsL and FtsQ in the predicted Mtb divisome structure (Fig. 1B); we suspected that this region was inessential for PerM-FtsB binding and that it might destabilize Mtb FtsB in the absence of Mtb FtsL and/or FtsQ. In these constructs, expression was induced by anhydrotetracycline (ATc), which is solvachromatic, and we confirmed that there was no significant background signal in our imaging conditions (Supplementary Fig. S3). Deletion of FtsB^{LQ} clearly increased the level of membrane-localized FtsB, suggesting instability of Mtb FtsB in the absence of FtsL and FtsQ. However, FtsB instability in Mtb may result from other mechanisms [9], so we did not investigate this in depth. We did not observe any further effect on mTurquoise2 fluorescence when deleting FtsB^H in addition to FtsB^{LQ}.

Conversely, initial attempts to construct mNeonGreen-labeled PerM failed for both N- and C-terminal fusion constructs (mNG-PerM and PerM-mNG; Fig. 3B). We manually inspected the predicted PerM structure as well as sequences of integral transmembrane protein orthologs in *E. coli* and Mtb, hypothesizing that an engineered construct, PerMⁿ¹, would exhibit higher expression. Specifically, we noticed an apparent “LK” motif in *E. coli* that rarely appeared in Mtb and was reminiscent of part of the twin-arginine translocation motif [26]. Our strategy in designing the PerMⁿ¹ construct was to modify PerM with aspects of the short LacY N-terminal sequence in ways that would not perturb the predicted PerM structure. While fluorescent protein expression was indeed much higher for PerMⁿ¹-mNG, it failed to exhibit the same degree of membrane localization as Pf3-mNG, which we used as a control given its efficient translocation and uniform transmembrane orientation [27].

We were surprised at how much the modifications in PerMⁿ¹ increased fluorescent protein expression levels and systematically investigated sequences in residues preceding the first predicted transmembrane helix in all proteins including at least one transmembrane helix in the *E. coli* and Mtb proteomes (Fig. 3C). We found large differences in the frequencies of some residues, most strikingly for differences in the relative frequencies of lysine

and arginine. Fig. 3D shows how this is reflected in orthologous sequences of FtsX as well as in PerMⁿ¹ compared to Mtb PerM. Finally, we proceeded to co-express PerMⁿ¹-mNG and mTq2-FtsB and look for evidence of PerM-FtsB interaction. Serendipitously, one of two adjacent *E. coli* microcolonies in a co-expression experiment lost the plasmid for mTq2-FtsB protein expression, which occasionally happened without including selective antibiotics in agarose gel pads (Fig. 3E). We note that we used a YFP filter set for mNeonGreen imaging to avoid crosstalk from mTurquoise2. The large difference in PerMⁿ¹-mNG membrane localization between these two microcolonies suggested an unexpected role for FtsB in stabilizing PerM in the *E. coli* membrane.

PerM stabilization in *E. coli* membrane by FtsB depends on FtsB^H

In order to confirm that FtsB increases membrane-localized PerM protein expression and, if so, to investigate the role of FtsB^H in this phenomenon, we co-expressed mNeonGreen- and mTurquoise2-labeled constructs and analyzed fluorescence in *E. coli* microcolonies (Fig. 4). In these experiments, expression of PerMⁿ¹-mNG was induced with 100 μ M IPTG. Localization controls mNeonGreen (strong cytoplasmic localization) and Pf3-mNG (strong membrane localization) were induced with 60 μ M and 240 μ M IPTG, respectively, to match typical PerMⁿ¹-mNG protein expression levels. Expression of mTurquoise2-labeled FtsB constructs was induced with 10 nM ATC in all conditions except for one condition with no induction (indicated with down arrow in Fig. 4). Brightfield images of *E. coli* cells were segmented, and protein concentration was estimated to be proportional to total integrated fluorescence after subtracting background and normalizing by cell size.

Relative to the reference condition (PerMⁿ¹ and FtsB^{ΔLQ}, 10 nM ATC), there was an 89% ($p = 3.3 \times 10^{-12}$) decrease in mTq2-FtsB^{ΔLQ} protein expression in the absence of induction, with no significant differences observed for other conditions. There was also no obvious difference in localization of any FtsB variant in any condition tested (Fig. 4B). The absence of any significant impact on full-length FtsB protein expression ($p = 0.97$) and the observation that PerMⁿ¹-mNG increases membrane localization of mTq2-FtsB (compare Fig. 4B and Fig. 3D to Fig. 3A) are consistent with the finding that PerM stabilizes FtsB [9] and that the

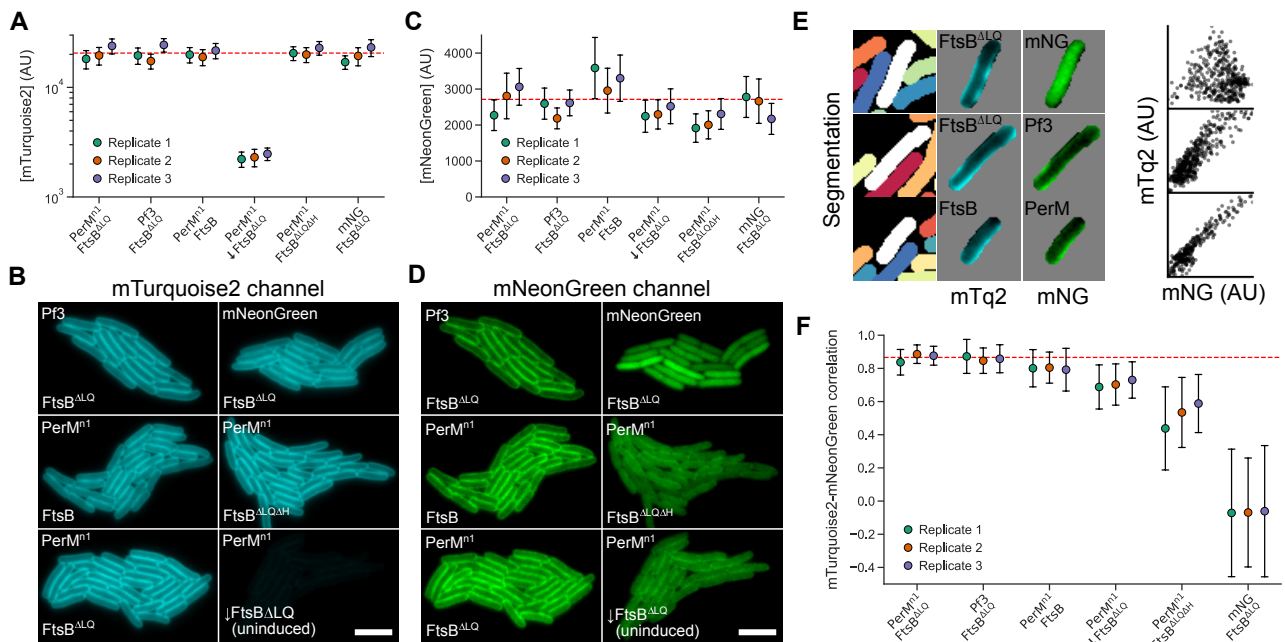


Fig. 4 FtsB stabilizes PerM in the *E. coli* membrane. (A) Distribution of single-cell mTurquoise2 concentration (mean \pm standard deviation) for FtsB constructs in different conditions, each with replicates. Dashed red line indicates the mean value for the reference condition (PerMⁿ¹-mNG, mTq2-FtsB^{ΔLQ}, 100 μ M IPTG, 10 nM ATC). Uninduced FtsB^{ΔLQ} is indicated with a down arrow. A logarithmic scale is used to allow comparison of high- and low-protein-expression conditions. (B) Example data from microcolonies for each condition. The uninduced FtsB^{ΔLQ} condition has very low fluorescence in example data because identical minimum and maximum intensities were used. Scale bar 5 μ m. (C, D) Distribution of single-cell mNeonGreen concentrations and example data for Pf3-mNG, mNeonGreen alone, or PerMⁿ¹-mNG in different conditions; prepared identically to A and B. (E) Left: example data analysis showing cell segmentation and isolated, single-cell intensities. Right: Scatter plots of single-pixel intensities for each cell show clear correlation for Pf3-mNG and PerM-mNG, but not for mNeonGreen alone. (F) Distribution of single-cell Spearman correlation coefficients (mean \pm standard deviation) for three replicates. Conditions ordered by decreasing mean correlation.

175 relative level of PerMⁿ¹-mNG in this experiment is sufficient for FtsB stabilization. However, we did not explore
176 this in detail given the lack of Mtb FtsL and FtsQ in our experimental system.

177 In contrast, there was a small reduction in PerMⁿ¹-mNG protein expression of 13.3% ($p = 3.8 \times 10^{-2}$) in
178 the absence of induction of mTq2-FtsB^{ΔLQ} protein expression, and a reduction of 23.5% ($p = 5.5 \times 10^{-4}$)
179 when FtsB^{ΔLQ} was replaced with FtsB^{ΔLQΔH}. There was no significant change when FtsB^{ΔLQ} was replaced
180 with wild-type FtsB ($p = 0.29$). This suggested that FtsB increased PerM stability in *E. coli*, and that this
181 depended on the presence of FtsB^H. However, inspection of Fig. 4C suggests that our sample size is overpowered
182 ($N = 10\,930$ cells in total from 3 replicates; 607 ± 44 cells per condition per replicate) given variation between
183 replicates in mNeonGreen protein expression levels. Clearly, total fluorescence intensity did not capture the
184 differences between conditions evident in Fig. 4D and an alternative method was required.

185 In preliminary experiments, we observed a large decrease in spatial correlation between mTurquoise2 and
186 mNeonGreen fluorescence when FtsB^{ΔLQ} was depleted or replaced by FtsB^{ΔLQΔH} (Fig. 4D). The observation
187 of small reductions in PerMⁿ¹-mNG levels despite apparently large impacts of different FtsB constructs on
188 localization suggested that fluorescent mNeonGreen often remained in the cytoplasm following PerMⁿ¹-mNG
189 degradation. We confirmed this by directly observing FtsB^H-dependent degradation of PerMⁿ¹-mNG in cell
190 extracts from samples differing in FtsB constructs and induction conditions; samples with mTq2-FtsB^{ΔLQΔH}
191 and uninduced samples with mTq2-FtsB^{ΔLQ} had a greater fraction of a major low-molecular-weight band as
192 well as a range of intermediate degradation products (Supplementary Fig. S4).

193 We hypothesized that quantifying spatial correlation would be a more sensitive measurement of PerMⁿ¹-
194 mNG stability than mNeonGreen fluorescence, both less susceptible to variation in protein expression levels and
195 robust against the presence of fluorescent, cytoplasmic PerMⁿ¹-mNG degradation products. Fig. 4E shows scatter
196 plots of mNeonGreen and mTurquoise2 intensities for pixels in typical cells with cytoplasmic mNeonGreen,
197 membrane-localized Pf3-mNG, and PerMⁿ¹-mNG. We calculated Spearman correlation coefficients from such
198 distributions for segmented cells and Fig. 4F shows the mean and standard deviation of correlation coefficients
199 for each condition and replicate.

200 In the reference condition (PerMⁿ¹-mNG, mTq2-FtsB^{ΔLQ}, 10 nM ATc), correlation was high ($\rho = 0.87$,
201 0.84–0.89 95% confidence interval) and indistinguishable from that when Pf3-mNG was expressed instead
202 ($\rho = 0.86$, 0.82–0.90). All other conditions had significant reductions in correlation. Wild-type FtsB was
203 marginally less well correlated ($\rho = 0.80$, 0.77–0.83). The apparent reductions in PerMⁿ¹-mNG protein expres-
204 sion levels discussed above were more strongly supported by analysis of spatial correlation, with a drop in
205 correlation in the absence of mTq2-FtsB^{ΔLQ} induction ($\rho = 0.71$, 0.69–0.73) and a larger drop when mTq2-
206 FtsB^{ΔLQ} was replaced with mTq2-FtsB^{ΔLQΔH} ($\rho = 0.52$, 0.46–0.58). While FtsB^{LQ} was not absolutely essential
207 for membrane localization of PerMⁿ¹, this was also observed in the absence of any FtsB expression (Fig. 3B).

208 Single-molecule FtsB tracking reveals that FtsB^H-dependent PerM binding

209 Our correlation analysis strongly suggested that FtsB interaction with PerM via FtsB^H is key for expression
210 of PerMⁿ¹ protein in the membrane. Since we observed this for transgenic expression in *E. coli*, it is unlikely
211 that PerM-FtsB interaction is mediated by host proteins. However, transient PerM-FtsB interaction could
212 be sufficient for PerM stability without a large fraction of molecules being bound at any time. If PerM is a
213 significant component in the core Mtb divisome as suggested by structure prediction, depletion phenotypes,
214 and midcell localization [8, 9], we hypothesized that this implied long-lived PerM-FtsB interactions that could
215 be detected by single-molecule tracking of FtsB diffusion. FtsB has a single transmembrane helix, while PerM
216 is predicted to have 8 (Fig. 1A); based on the dependence of diffusion of integral membrane proteins on the
217 number of transmembrane helices, we expected a reduction in the FtsB diffusion coefficient from approximately
218 0.7 to $0.3 \mu\text{m}^2 \text{s}^{-1}$ upon PerM binding [28].

219 We constructed mEos3.2-tagged variants of FtsB^{ΔLQ} and FtsB^{ΔLQΔH}, and co-expressed them with either
220 PerMⁿ¹-mNG or Pf3-mNG. Fig. 5A shows a typical frame from single-molecule imaging data, localized mEos3.2
221 molecules, and single-molecule tracks gathered in one movie showing that tracked molecules were detected near
222 the middle plane of *E. coli* cells (approximately 0.5 μm from the microscope coverslip). In analysis of preliminary
223 data, we found that analysis of either mean squared displacement or fitting jump-length distributions was
224 sensitive to variable trajectory length. Thus, we utilized SASPT [29] to infer distributions of *apparent* diffusion
225 coefficients using a method robust against short trajectories, variable localization error, and defocalization [30].
226 Note that we refer to an *apparent* diffusion coefficient, as diffusion within our images is largely confined to
227 the one-dimensional perimeter at the middle plane and, further, confined at the cell poles. So, while this is
228 sufficient to compare relative diffusion rates in different conditions, precise estimates of diffusion coefficients
229 will require more sophisticated methods and would benefit from 3D tracking over the entire membrane.

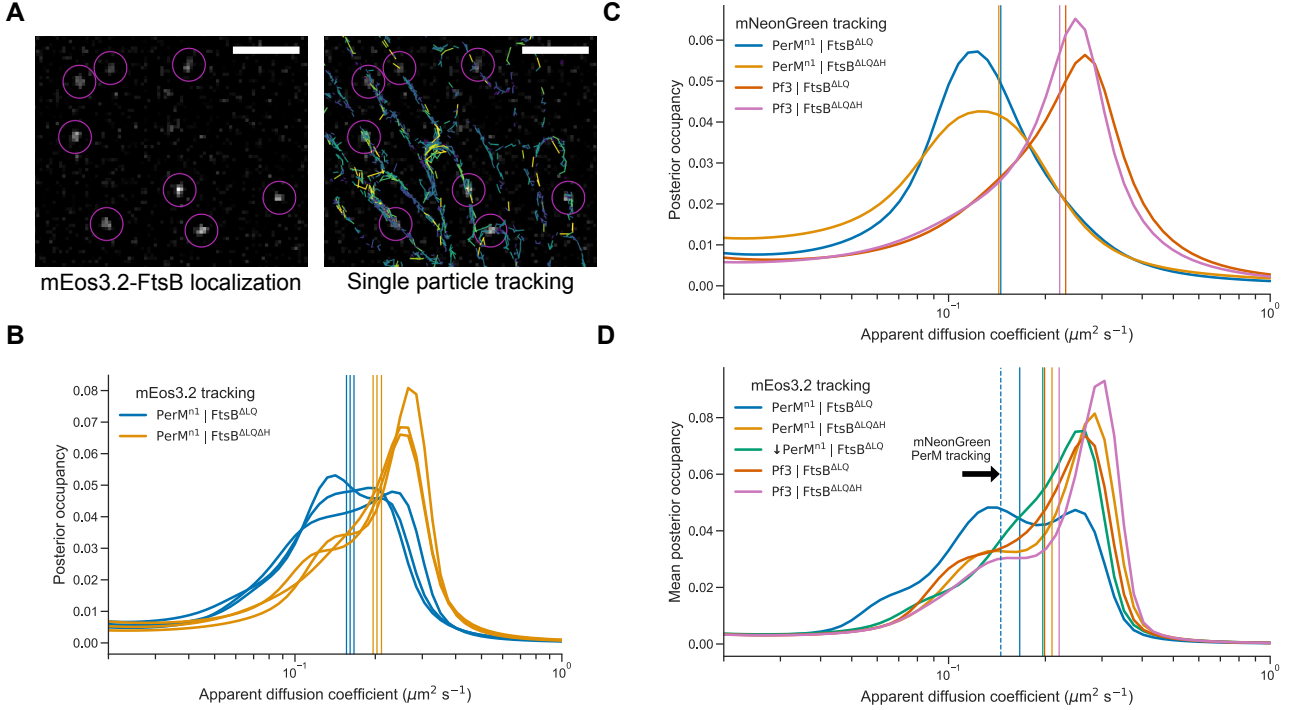


Fig. 5 PerM-FtsB binding detected by FtsB single-molecule tracking. (A) Left: single, 33-ms frame from a fluorescence microscopy movie of mEos3.2-FtsB^{ΔLQ} diffusion in *E. coli*. Right: Single-molecule localization and tracking results for the entire movie show membrane-localized diffusion. Scale bar 2 μm . (B) Posterior occupancies in a model of regular Brownian motion and localization error were marginalized over localization error to estimate the distribution of apparent 2D diffusion coefficients. Distributions and their means (vertical lines) are shown for three replicates of experiments combining PerMⁿ¹-mNG with either mEos3.2-FtsB^{ΔLQ} or mEos3.2-FtsB^{ΔLQΔH}. (C) Estimated distributions of diffusion coefficients inferred from single-molecule tracking of either PerMⁿ¹-mNG or Pf3-mNG with either FtsB^{ΔLQ} or FtsB^{ΔLQΔH} (single experiment). Vertical lines indicate the mean estimated diffusion coefficient for each condition. (D) Estimated distribution of diffusion coefficients for either mEos3.2-FtsB^{ΔLQ} or mEos3.2-FtsB^{ΔLQΔH} co-expressed with either Pf3-mNG or PerMⁿ¹-mNG (with or without addition of 100 μM IPTG), inferred from combining data from three replicates. Vertical lines indicate mean estimated diffusion coefficients and the dashed vertical line is replicated from C.

230 In tracking experiments, mEos3.2-FtsB constructs were expressed without induction so that PerM would be
 231 in excess and maximize potential binding. We inferred distributions of diffusion coefficients after marginalizing
 232 out localization error for three independent replicates (Fig. 5B). We observed reproducible differences in mean
 233 diffusion coefficients between FtsB^{ΔLQ} ($0.161 \pm 0.004 \mu\text{m}^2 \text{s}^{-1}$; mean \pm standard deviation) and FtsB^{ΔLQΔH}
 234 ($0.203 \pm 0.006 \mu\text{m}^2 \text{s}^{-1}$; mean \pm standard deviation). Distributions for both FtsB^{ΔLQ} and FtsB^{ΔLQΔH} suggested
 235 the presence of a slow-diffusion population at approximately $0.14 \mu\text{m}^2 \text{s}^{-1}$ that is more prominent for FtsB^{ΔLQ}.
 236 We also collected single-molecule tracking data for PerMⁿ¹-mNG and Pf3-mNG in single experiments. Despite
 237 limitations of this data (fewer localizations and variable spot density as mNeonGreen photobleaches over time),
 238 we inferred average diffusion coefficients of $0.144 \mu\text{m}^2 \text{s}^{-1}$ and $0.226 \mu\text{m}^2 \text{s}^{-1}$ for mNG-PerM and mNG-Pf3,
 239 respectively (Fig. 5C).

240 To estimate the most likely apparent diffusion coefficients, we inferred distributions from all data from
 241 each condition (Fig. 5D). This confirmed that mEos3.2-FtsB^{ΔLQ}, when expressed with PerM, clearly exhibits
 242 slower diffusion than when PerM is replaced with Pf3 or in the absence of FtsB^H. Peaks at approximately
 243 0.14 and $0.25 \mu\text{m}^2 \text{s}^{-1}$ are consistent with a substantial decrease in the rate of diffusion upon PerM binding.
 244 Compared to conditions with mEos3.2-FtsB^{ΔLQΔH} and conditions with Pf3, mEos3.2-FtsB^{ΔLQ} in the absence
 245 of induction of PerMⁿ¹-mNG exhibited the slowest diffusion (green line in Fig. 5D). This indicated that low-
 246 level PerMⁿ¹-mNG in the absence of induction has substantial mEos3.2-FtsB^{ΔLQ} binding. However, the effect
 247 size was clearly low and further work is required to determine the concentration dependence of this interaction.

248 PerM-FtsB interaction could restrict conformational flexibility of the Mtb 249 divisome

250 Our observation that FtsB^H-dependent PerM-FtsB interaction was sufficiently long-lived to produce large
 251 changes in FtsB diffusion prompted us to explore how this interaction could impact the Mtb divisome. We

conducted MD simulations to compare divisome constructs in which FtsB was truncated to FtsB²⁰⁵ (removing the uncertain C-terminal residues) or truncated to FtsB¹⁸⁵ (additionally remove FtsB^H). First, we performed MD for the Mtb divisome with PerM and full-length FtsB for 500 ns. FtsB N-terminal residues and other terminal residues of subunits without confident structure predictions were omitted. A period of initial MD was required since our structure prediction did not have all subunits at ideal relative orientations; this was especially significant for FtsQ since its transmembrane helix is distant from others. The final conformer after 500 ns was used to build systems with truncation to FtsB²⁰⁵ (FtsB^{ΔC}) and to FtsB¹⁸⁵ (FtsB^{ΔCΔH}), and each system was simulated for 1 μs. The final conformer for FtsB^{ΔC} is shown in Fig. 6A.

Comparing the final conformers of the FtsB^{ΔC} and FtsB^{ΔCΔH} simulations, we examined the angle formed as the vector between the putative active site residues FtsW^{D311} and PbpB^{S386} rotates during MD simulation (Fig. 6B). This angle is a proxy for the tilt of the PbpB transpeptidase domain relative to FtsW that has been used to analyze Cryo-EM data as well as MD simulation. We observed a 19.2° tilt for FtsB^{ΔC}, similar to that observed for *P. aeruginosa* FtsI comparing a structure prediction to its Cryo-EM structure [19] and for *E. coli* comparing a structure prediction to conformers following MD [20]. Conversely, with the loss of PerM-FtsB interaction mediated by FtsB^H, the tilt angle reverted to a value within only 4.8° of the predicted structure. The progression of these angles over the course of MD is shown in Fig. 6C.

Relative to studies on the divisome in model organisms, there is a paucity of experimental data to relate our simulations to phenotypes associated with mutations to Mtb divisome components. Thus, we did not analyze interactions between Mtb divisome subunits in depth or conformations in and around FtsW and PbpB active sites. However, we note substantial differences the relative conformations of divisome components in final conformers for the FtsB^{ΔC} and FtsB^{ΔCΔH} simulations; tilt of the PpbB transpeptidase domain was associated

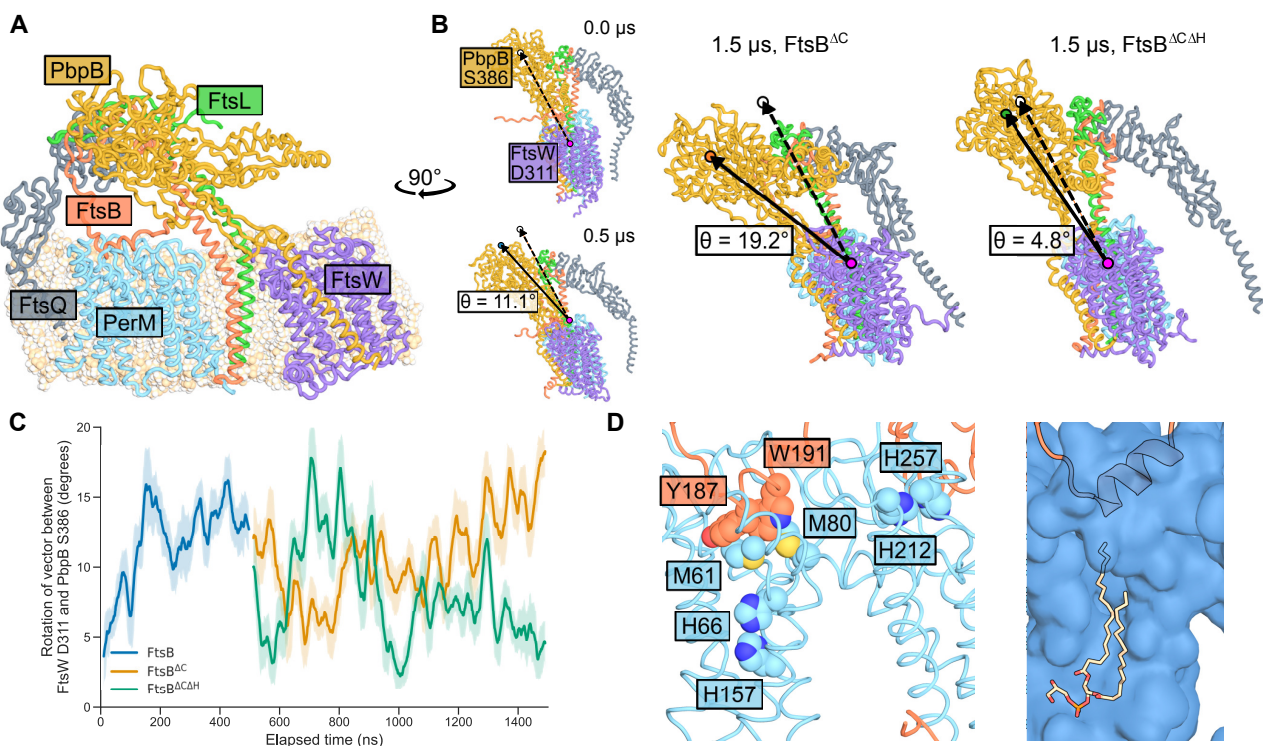


Fig. 6 PerM-FtsB interaction constrains the Mtb divisome in MD simulations. (A) PerM simulated in context of Mtb divisome. Final conformer after 0.5 μs of MD with full-length FtsB followed by 1 μs of MD with FtsB^{ΔC}. Note C-terminal truncation of FtsB relative to the predicted structure in Fig. 1A that is uncertain in this region. (B) Difference in tilt of PpbB transpeptidase domain relative to its conformation in structure prediction. Left: initial and final conformers of a 500 ns simulation including FtsB C-terminal residues. Locations of putative active-site residues FtsW^{D311} and PpbB^{S386} and the vector between them are highlighted; tilt of PpbB relative to FtsW is quantified by rotation of this vector. All conformers are aligned by FtsW Cα atoms. The final conformer of the 500 ns simulation was used as the initial conformation for subsequent simulations. Right: Final conformers for FtsB^{ΔC} and FtsB^{ΔCΔH} simulations are shown along with their associated tilt angles. (C) Dynamics of tilt angles defined in B show that the FtsB^{ΔCΔH} simulation returned towards the elongated conformation observed in structure predictions. A 25 ns moving average of the tilt angle is shown and shaded areas indicate one standard deviation above and below the average angle. Line colors correspond to colors of circles in B. (D) Final conformer of PerM-FtsB aMD simulation after 1.1 μs. Left: residues in PerM near FtsB-binding interfaces suggest that PerM could potentially be sensitive to environmental cues. Right: a lipid often fills a channel in PerM in MD; here, in the final conformer of the aMD simulation, a phosphatidylglycerol molecule interacts with FtsB^H.

273 with twisting of the PbpB head domain, FtsL, and FtsQ relative to FtsW. Lastly, in Fig. 6D we return to the
274 final conformer of a PerM-FtsB simulation following aMD to highlight residues of interest in PerM that are
275 suggestive of potential regulatory mechanisms. We also show how a phosphatidylglycerol molecule occupies a
276 channel in PerM and interacts with FtsB^H.

277 Discussion

278 With our integrative approach combining fluorescence microscopy with molecular dynamics starting from pre-
279 dicted structures of protein complexes, we showed that FtsB^H directly mediates PerM-FtsB binding. Our results
280 suggest that significance of PerM-FtsB interaction goes beyond FtsB stabilization [9] to potentially impacting
281 the structure of the core Mtb divisome. Given the role of PerM in persistent Mtb infection and that it is
282 essential in *M. smegmatis*, it will be interesting to learn whether FtsB also stabilizes PerM in mycobacteria, as
283 it does in *E. coli*, and whether the PerM-FtsB interaction that we have identified can be targeted to disrupt
284 regulation of cell division.

285 Our approach is straightforward to apply to other predicted protein-protein interactions. For example, Mtb
286 PerM is located in the same operon as Rv0954 which similarly localizes to the Mtb divisome yet has no reported
287 deletion phenotype [31]. Intriguingly, while PerM is associated with the divisome component FtsB, Rv0954
288 exhibited physical and genetic interactions with elongasome components such as RodA and PbpA. However,
289 division and elongation machinery in mycobacteria are not perfectly analogous to those in other bacteria [32].
290 The cell-stress phenotypes of PerM depletion in Mtb suggest that conditional phenotypes may be identified for
291 Rv0954 as well.

292 In Fig. 6D, we highlight PerM residues that could play roles in integrating environmental stress in proximity
293 to FtsB^H. These include buried histidines that are intriguing with respect to the Mg²⁺-dependent phenotype of
294 PerM, suggesting sensitivity to nutrient depletion [8], methionine residues that make hydrophobic interactions
295 with FtsB^H and could be sensitive to oxidation, and histidine residues near the membrane surface that could
296 sensitize PerM-FtsB interaction to pH. Furthermore, in MD we routinely observed lipids to penetrate the first
297 half of PerM and come into contact with FtsB, suggesting the possibility that bilayer composition can directly
298 impact PerM-FtsB interaction.

299 In our experimental system, transgenic expression of Mtb PerM and FtsB proteins in *E. coli* makes it likely
300 that we observed effects of direct PerM-FtsB interaction. This is an advantage of our system as it suggests
301 that PerM-FtsB binding does not depend on phosphorylation or other post-translational modification specific
302 to mycobacteria. While our single-molecule tracking experiments are not easily extensible to high-throughput
303 investigation, PerM-FtsB and other Mtb protein-protein interactions can be explored by adopting our approach
304 to develop FRET interaction reporters based on structures of predicted complexes. It will also be interesting to
305 see whether our anecdotal success in engineering improved membrane protein expression in *E. coli* is applicable
306 to other Mtb membrane proteins.

307 Our approach also carries the inevitable limitations of exploring an interaction in a surrogate system. It
308 is critical to not extrapolate too much from our experiments before confirming results in Mtb. Our models
309 of the Mtb divisome make countless predictions that are testable given the variety of tools for manipulating
310 mycobacterial gene expression and recombineering. Additionally, our MD simulations omitted terminal residues
311 in divisome components that are likely functional in some cases. This is only one example of interactions
312 that we did not predict, but also cannot rule out. As another example, a specific FtsB-PerM interface in the
313 membrane was not predicted and did not emerge in MD, but chimeras replacing FtsBTM with an alternative
314 transmembrane helix could determine whether it contributes to PerM binding. One prediction arising from our
315 work is that overexpression of FtsB^H in the Mtb or *M. smegmatis* periplasm could produce PerM-depletion
316 phenotypes [9] via competitive inhibition of PerM-FtsB interaction.

317 Lastly, our observation that PerM-FtsB interaction constrains PbpB in a tilted conformation can be con-
318 sidered in light of results and discussion emerging from the Cryo-EM structure of the *P. aeruginosa* divisome
319 [19], where an elongated conformation was considered to potentially reflect the catalytically active state. Recent
320 work combining *in vitro* single-molecule and peptidoglycan polymerization assays with characterization of *in*
321 *vivo* phenotypes supported this model for the gram-negative elongasome [33]. Within the context of this model
322 and in light of our results, the role of PerM would be to reduce divisome activity by constraining PbpB in a con-
323 formation with relatively low transpeptidase activity. This is an apparent paradox given that PerM is essential
324 in some conditions in Mtb and in *M. smegmatis*. However, the paradox can be resolved if PerM plays both a
325 role in promoting FtsB stability (which can be bypassed with FtsB overexpression [9]) and also a conditionally
326 essential role in regulating divisome activity that could contribute to persistent Mtb infection.

327 Methods

328 Structure prediction

329 PerM and FtsB sequences used for structure prediction are listed in Table 1 and additional Mtb sequences used
330 for complex structure prediction are listed in Table 2. FtsB and PerM were identified in various actinomycete
331 species and, after multiple sequence alignment, have between 19 % and 61 % (PerM) and 27 % and 62 % (FtsB)
332 amino acid identity with Mtb orthologs. Protein complex structures were predicted using ColabFold [34].
333 Multiple sequences alignments were provided by MMseqs2 [35] using both paired and unpaired sequences in
334 reference and environmental sequence databases. AlphaFold-Multimer [16] (Version 3, Model 4, 12 recycles)
335 was used for structures compared in Fig. 1 and Supplementary Fig. S1 and for structure predictions utilized
336 to build MD systems. PyMOL [36] was used for all structure visualizations and its align function was used to
337 align FtsW structures and to calculate RMSD (using cycles=0).

338 Sequence analysis

339 To compare PerM and FtsB for different species, multiple sequence alignments were generated using Clustal
340 Omega [37] and visualized using Biotite [38]. To compare amino acid frequencies at transmembrane helices, we
341 used DeepTMHMM [39] to predict the positions of the first transmembrane helix for all proteins in reference
342 proteomes for *E. coli* and Mtb (UniProt ID UP000000625 and UP000001584). Amino acid frequencies and
343 corresponding sequence logos for the 10 residues preceding the first residue in the first predicted transmembrane
344 helix were calculated and plotted using Logomaker [40].

345 Molecular dynamics

346 Molecular dynamics systems were constructed from structures of predicted complexes (or from the final con-
347 former of the initial 500 ns divisome complex simulation) with the CHARMM-GUI Membrane Builder [41].
348 Shared simulation parameters chosen in CHARMM-GUI were: 150 mM KCl, CHARMM36m forcefield [42],
349 310 K temperature, NPT ensemble, and capping all non-native N- and C-terminal residues with ACE and CT3,
350 respectively. Scripts for OpenMM [43] output by CHARMM-GUI were modified and OpenMM was used for
351 MD simulation. Simulation system sizes are detailed in Table 3.

352 Simulation systems differed in a few ways (other than small differences in residues included, shown in
353 Table 4). First, bilayers simulations for the PerM-FtsB complex and PerM alone included a 3:1 POPE:POPG
354 ratio commonly used for simulations of *E. coli* membranes since MD results were compared to *E. coli* microscopy

Table 1 GenPept accession numbers for PerM and FtsB sequences used for different actinomycete species.

Species	PerM accession	FtsB accession
<i>Mycobacterium tuberculosis</i>	NP_215470	NP_215540
<i>Mycobacterium smegmatis</i>	WP_011730590	WP_029104417
<i>Mycobacterium trivialis</i>	WP_085109558	WP_085109605
<i>Mycobacterium terrae</i>	WP_085262653	WP_085262505
<i>Mycobacteroides abscessus</i>	WP_012296377	WP_005066469
<i>Nocardia asteroides</i>	WP_022566234	WP_019049142
<i>Gordonia bronchialis</i>	WP_012833219	WP_041919790
<i>Corynebacterium diphtheriae</i>	WP_014318836	WP_021334958
<i>Actinosynnema pretiosum</i>	WP_157767928	WP_253846810
<i>Actinopolyspora halophil</i>	WP_026152723	WP_017976585

Table 2 GenPept accession numbers of other Mtb division components used in this study.

Protein	Accession
FtsQ	NP_216667
FtsL	NP_216680
FtsW	NP_216670
PbpB	NP_216679

Table 3 Number of total atoms and numbers and types of lipid residues in MD systems.

System	Atoms	Residues	
		POPE	POPG
PerM-FtsB	156168	210	70
PerM only	105155	213	71
Complex (FtsB)	724208	1246	—
Complex ($FtsB^{\Delta C}$)	709754	1239	—
Complex ($FtsB^{\Delta C \Delta H}$)	709645	1239	—

355 data. Simulations for divisome complexes used pure POPE bilayers, and future work may investigate differences
 356 in more complex model membranes [44]. Second, simulations of the PerM-FtsB complex and PerM alone fol-
 357 lowed a three-stage aMD protocol described in the main text with 2 fs timesteps. For the aMD stage, OpenMM
 358 scripts from CHARMM-GUI [45] were modified to utilize empirically determined dual boost potentials as pre-
 359 viously described for MD of transmembrane proteins [46] and to output a log of applied boost potentials. We
 360 monitored boost potentials applied to dihedral angles and total energy and found the magnitudes of the two
 361 boost potentials were similar. For the final two simulations depicted in Supplementary Fig. S2, the λ parame-
 362 ter used to calculate the dihedral boost reference energy and acceleration factor was reduced from 0.3 to 0.15.
 363 Lastly, divisome complex simulations utilized hydrogen mass repartitioning [47] and 4 fs timesteps.

364 Atoms of interest for analysis shown in Fig. 2B and Fig. 6C were identified by investigating sequence
 365 alignments to orthologs of FtsB, PbpB, and FtsW to determine conserved $FtsB^H$ residues and putative active-
 366 site residues. The MDAnalysis package [48, 49] was used to extract trajectories wrapped around the center of
 367 mass of protein atoms, to align divisome complex trajectories to $FtsW^{60-407}$ (omitting more mobile cytoplasmic
 368 residues), and to extract atomic coordinates. All-atom coordinates of initial and final conformers as well as
 369 protein-only trajectories are available as supplementary data.

370 *E. coli* strain construction

371 In addition to Mtb PerM and FtsB (and variations described in the main text), capsid protein G8P from
 372 bacteriophage Pf3 (UniProt identifier P03623; referred to as “Pf3” elsewhere in this manuscript) was uti-
 373 lized as a control based upon its small size, efficient translocation, and uniform transmembrane orientation
 374 [27]. Proteins were expressed as translational fusions with fluorescent proteins mTurquoise2 [25], mNeonGreen
 375 [24], or mEos3.2 [50]. No linkers were added between Mtb protein sequences and fluorescent proteins as we
 376 expected that native termini were disordered based on structure predictions. Sequences for all proteins were
 377 codon-optimized for *E. coli* protein expression. Plasmids for FtsB-expressing constructs were constructed
 378 by isothermal assembly from low-noise, tetracycline-inducible, ampicillin-resistant vectors [51]. Plasmids for
 379 expression of mNeonGreen as well as mNeonGreen fusions to PerM variants and Pf3 were constructed from
 380 IPTG-inducible, spectinomycin-resistant vectors [52]. All plasmids and induction conditions used in this study
 381 are summarized in Table 5.

382 Plasmids were transformed into *E. coli* strain MG1655 and selected for growth on 50 mg L⁻¹ carbenicillin
 383 and/or spectinomycin in LB or SOB media. For microscopy experiments, cells were grown overnight from LB
 384 plates in rich defined medium [53] with 0.2% glucose (ForMedium Neidhardt Basal Salt Mixture, Glucose
 385 20 g L⁻¹, and Neidhardt Supplement Mixture, Complete), adjusted to pH 7.0 with KOH. All cell growth and
 386 imaging took place at 37 °C. Consistent with our earlier work, our plasmids allowed for independent induction

Table 4 Residues included in MD simulation systems.

Component	PerM-FtsB and PerM only	FtsB	Divisome systems	
			$FtsB^{\Delta C}$	$FtsB^{\Delta C \Delta H}$
PerM	11–390	10–385	10–385	10–385
FtsB	61–204	74–228	74–205	74–185
FtsQ	—	92–314	92–314	92–314
FtsL	—	120–232	120–232	120–232
FtsW	—	41–456	41–456	41–456
PbpB	—	79–679	79–679	79–679

Table 5 *E. coli* plasmids utilized in this study and their respective induction conditions. Mutations are described relative to wild-type Mtb protein sequences in Table 1 and Table 2

Plasmid	Selection	Induction	Expressed protein	Mutation
pJRF002	Carbenicillin	10 nM ATc	mTq2-FtsB	—
pJRF007	Carbenicillin	10 nM ATc	mTq2-FtsB ^{ΔLQ}	FtsB ^{Δ111-163}
pJRF007_helix	Carbenicillin	10 nM ATc	mTq2-FtsB ^{ΔLQΔH}	FtsB ^{Δ111-163Δ186-194}
pZH904	Carbenicillin	10 nM ATc	mEos3.2-FtsB ^{ΔLQ}	FtsB ^{Δ111-163}
pLG906	Carbenicillin	10 nM ATc	mEos3.2-FtsB ^{ΔLQΔH}	FtsB ^{Δ111-163Δ186-194}
pJRF001	Spectinomycin	100 μM IPTG	mNG-PerM	—
pJRF004	Spectinomycin	100 μM IPTG	PerM-mNG	—
pJRF004_n1_cWT	Spectinomycin	100 μM IPTG	PerM ⁿ¹ -mNG	PerM ^{Δ1-23} :MYYLKNLVK
pJRF010	Spectinomycin	240 μM IPTG	Pf3-mNG	—
pZH813	Spectinomycin	60 μM IPTG	mNeonGreen	—

387 of co-expressed genes [52]. In preliminary experiments, we confirmed that mTurquoise2- and mNeonGreen-
388 labeled proteins could be independently induced, that inducing protein expression did not impact growth at
389 expression levels utilized in this work, and that there was no significant crosstalk between mTurquoise2 (CFP
390 filter set) and mNeonGreen (YFP filter set).

391 Fluorescence microscopy

392 All imaging was done on a Leica DMI6000 inverted microscope using illumination from either a Leica EL6000
393 source or with laser excitation at 514 nm (mNeonGreen tracking) or combined 405 nm and 561 nm laser exci-
394 tation (mEos3.2 tracking), adjusting 405 nm laser intensity to achieve acceptable densities of photoactivated
395 mEos3.2 molecules. Data was acquired using a 100×/1.46 a-plan apochromat oil immersion objective with
396 additional 1.6× magnification, Leica type F immersion oil, and an Evolve 512 EM-CCD camera (Photomet-
397 rics), giving a 100 nm pixel size and a narrow depth of field. Fluorescence images were acquired with three
398 different filter sets: Chroma 49001 (mTurquoise2), Semrock LF514-B (mNeonGreen), and a Chroma custom
399 dual-laser filter set (mEos3.2; ZET405/561x, ET610/75m, ZT405/561/657rpc-UF2). Images of example data
400 were composed using Fiji [54], with linear scaling and maintenance of minimum and maximum intensity values
401 for all comparable images.

402 Microscope samples were prepared by sandwiching agarose gel pads (rich, defined media with 2% Invitrogen
403 UltraPure agarose) of approximately 100 μL between microscope slides and acid-cleaned #1.5H coverslips
404 (Marienfeld). For all experiments, samples were reinoculated from overnight cultures at a 1:1000 dilution in
405 media including IPTG and/or ATc at specified concentrations, grown for 3 h, added to a gel pad prepared
406 from the same media, and grown for an additional 1.5 h before acquiring data. Microscope sample temperature
407 was held at 37 °C using a combination of a heated microscope sample chamber and an objective heater. This
408 protocol was based on empirical observations that cells reached steady state fluorescence and growth in less
409 than 1 h after sample preparation, and that excessive cell density led to reduced growth and fluorescence after
410 approximately 3 h. In preliminary experiments, we also noted that this combination of growth media and
411 agarose exhibited high background with substantial variation between experiments, found that this could be
412 attributed to agitation while melting agarose. We subsequently minimized agitation while preparing gel pads.

413 To obtain comparable data for constructs expected to have different translation initiation rates, we con-
414 ducted preliminary experiments and determined that 60 μM and 240 μM IPTG induction for plasmids expressing
415 mNeonGreen and Pf3-mNG, respectively, were approximately equivalent to 100 μM IPTG for plasmids express-
416 ing PerMⁿ¹-mNG. Protein expression was always induced with IPTG and ATc concentrations listed in Table 5
417 except in the uninduced conditions indicated by down arrows in figures. To increase reproducibility in fluores-
418 ce correlation and single-molecule tracking analysis, we aimed to image the middle plane of *E. coli* cells
419 approximately 500 μm from the microscope coverslip. For fluorescence correlation analysis, we obtained images
420 of 20 fields of cells for each condition in each of 3 independent replicates. For single-molecule tracking analysis,
421 we obtained streaming movies (33 ms exposure time) of 5 fields of cells for each condition in each of 3 indepen-
422 dent replicates (except for mNeonGreen tracking for which we did not replicate the experiment). Replicates
423 were obtained on separate days, and sample preparation steps were staggered in time to minimize differences
424 in how samples were handled for each condition.

425 Fluorescence correlation analysis

426 Brightfield images were segmented using Omnipose [55]. The low and variable contrast in our brightfield data
427 produced variation in widths of segmented objects, so objects were morphologically thinned to single-pixel
428 width and then thickened to a uniform width that was more consistent with observed cell morphology. Sub-
429 pixel channel alignment was achieved by maximizing pairwise cross-correlation of low-pass filtered fluorescence
430 images with inverted brightfield images (*i.e.* mTurquoise2 and mNeonGreen images were aligned to brightfield
431 images—not to each other). Background intensity was estimated as the mode of a histogram of low-intensity
432 pixels outside of *E. coli* cells; in all conditions including uninduced mTq2-FtsB^{ΔLQ}, cellular autofluorescence
433 was very low relative to signal from fluorescent proteins. Fluorescence intensities in pixels corresponding to
434 segmented cells after alignment and background subtracted were compared as described in the main text.

435 For mNeonGreen and mTurquoise2 concentration and correlation comparisons, a mixed linear model was fit
436 to data points from single cells with random slopes and intercepts to allow for day-to-day variation. Two-tailed
437 p-values were calculated for comparison to the reference condition (PerMⁿ¹ and FtsB^{ΔLQ}, 100 nM ATc) and
438 adjusted for multiple comparisons using the Holm-Šidák method. Effect sizes are reported for significant results
439 only (adjusted $p < 0.05$). Unless stated otherwise, errors in the manuscript are 1 standard error of the mean. We
440 followed our designed analysis protocol and manually screened data to identify and exclude image fields that
441 could contribute to outliers (large shifts in sample position, poor focus, or unusual levels of fluorescent protein
442 expression for one or both proteins in a microcolony; 32 of 360 total images) and also excluded cells falling
443 outside the middle 95th percentile in either fluorescence intensity or cell area. However, we found that removing
444 all data filtering steps did not significantly impact differences we observed between experimental conditions.

445 Direct observation of FtsB-dependent PerMⁿ¹-mNeonGreen degradation

446 Strains expressing PerMⁿ¹-mNeonGreen together with either mTurquoise2-FtsB^{ΔLQ} or mTurquoise2-
447 FtsB^{ΔLQΔH} were cultured overnight in 1 mL of rich defined medium supplemented with 50 mg L⁻¹ spectino-
448 mycin and carbenicillin. Overnight cultures were diluted 1:1000 into 5 mL of fresh media of the same composition
449 with the addition of different inducers (100 μM IPTG, 10 nM ATc, or both). After a 3 h incubation at 37 °C,
450 the cells were harvested by centrifugation (8000 g, 1 min, 4 °C) and washed twice with pre-cooled PBS. Following
451 the final wash, the cells were resuspended in lysis buffer (PBS, 1 mg mL⁻¹ lysozyme, 1×cComplete protease
452 inhibitor cocktail (Roche), 1% Triton X-100) and sonicated for 10 min using in cycles of 30 s on and 30 s off
453 using a Bioruptor Plus sonication device. Cell lysates were mixed with 3×sample loading buffer (187.5 mM Tris,
454 6% SDS, 30% glycerol, 0.03% bromophenol blue, pH 7) and 30×DTT (1.25 M). Samples were not heated in
455 order to maintain mNeonGreen fluorescence [56]. Proteins were separated by Tris-Glycine-SDS electrophoresis
456 (12% acrylamide) together with a prestained ladder (Bio-Rad Precision Plus Dual Color). The gel was rinsed in
457 water and imaged using an iBright FL1500 to observe mNeonGreen and mTurquoise2 signals in two channels.
458 One channel detected both mTurquoise2 and mNeonGreen (455 nm to 485 nm excitation and 508 nm to 557 nm
459 emission) and the other channel detected mNeonGreen with extremely low mTurquoise2 efficiency (490 nm to
460 520 nm excitation and 568 nm to 617 nm emission). The relative degree of PerMⁿ¹-mNeonGreen degradation
461 was estimated as the fraction of the major high- and low-molecular weight bands observed in the low-molecular
462 weight band compared to the mTurquoise2-FtsB^{ΔLQ} condition with 10 nM ATc.

463 Inference of diffusion coefficient distributions

464 We extracted single-molecule trajectories from image stacks using TrackMate [57]. Spots were detected using
465 DogDetector (250 nm spot radius) and tracked using SimpleSparseLAPTracker (500 nm maximum linking
466 distance). Thresholds were determined empirically for mEos3.2 (160) and mNeonGreen (200) data, and the first
467 250 frames of mNeonGreen movies were omitted to exclude data before sufficient photobleaching had occurred
468 to acquire single-molecule tracks of mNeonGreen molecules. Trajectories were 3.56 ± 0.03 and 3.65 ± 0.11
469 frames long for mEos3.2 and mNeonGreen, respectively (mean and standard error of the means for 15 mEos3.2
470 and 4 mNeonGreen experiments; 5 streaming movies acquired in each experiment). We then used SASPT
471 [29] to infer posterior distributions of track diffusion coefficients and localization errors, marginalizing out
472 localization distributions for analysis related to Fig. 5. Posterior distributions were inferred for log-spaced
473 diffusion coefficients between 0.01 and 10 μm² s⁻¹. Distributions were normalized to occupancies between 0.02
474 and 1 μm² s⁻¹ to exclude states with highly variable occupancy at the extremes of the diffusion coefficient range.

475 Our primary analysis used default SASPT parameters (200 iterations of refining state occupancy, trajectories
476 longer than 10 frames split into trajectories 10 frames long or less) and we increased the `sample_size` parameter
477 to avoid subsampling data. Based on our observation that single-molecule tracks clearly show the perimeter

478 of *E. coli* cells at the middle plane, we used 500 nm for the `focal_depth` parameter. We also note that we
479 manually inspected maximum projections of all image stacks to verify that cells were well focused. To check for
480 sensitivity to SASPT analysis parameters, we repeated posterior occupancy inference with various conditions:
481 (1) excluding trajectories that were relatively long (> 10 frames which can arise from fluorescent objects
482 that do not photobleach) or short (2-frame trajectories that can arise from false positive localizations), (2)
483 fixing localization error to 25 nm, and (3) increasing state array refinement to 1000 iterations. We found that
484 SASPT results were robust against parameter choices and that the largest difference was somewhat narrower
485 distribution peaks with increased iterations.

486 **Acknowledgements.** ZH is supported by Fundação para a Ciência e a Tecnologia (FCT) through
487 MOSTMICRO-ITQB (DOI 10.54499/UIDB/04612/2020; DOI 10.54499/UIDP/04612/2020) and LS4FUTURE
488 Associated Laboratory (DOI 10.54499/LA/P/0087/2020). ZH and RX are supported by a MOSTMICRO-
489 ITQB Exploratory Projects grant. ZH and JRF thank Sara F. Costa for assistance and insight on this project.
490 ZH thanks Luísa Guerreiro and Margarida Pereira who worked on this project during internships in our lab.

491 **Data availability.** Plasmids described in this manuscript will be made available through AddGene. Data
492 and analysis notebooks are available on request and will be made available upon publication at <https://github.com/smmlab/mtb-perm-ftsb>. Raw microscopy data and MD trajectories (protein atoms only) will be deposited
493 at the Zenodo repository shortly and can be found by visiting the URL above.

495 **Author contributions.** JF: molecular cloning, data acquisition, preliminary data analysis and interpretation.
496 RX: data acquisition, methods development, data analysis. ZH: structure predictions and simulation, data
497 acquisition, data analysis. All authors wrote and edited the manuscript.

498 References

- 499 [1] Houben, R. M. G. J. & Dodd, P. J. The Global Burden of Latent Tuberculosis Infection: A Re-estimation
500 Using Mathematical Modelling. *PLOS Medicine* **13**, e1002152 (2016). <https://doi.org/10.1371/journal.pmed.1002152>.
- 502 [2] WHO. Latent tuberculosis infection: Updated and consolidated guidelines for programmatic management.
503 Tech. Rep. (2018).
- 504 [3] Dale, K. D. *et al.* Quantifying the rates of late reactivation tuberculosis: A systematic review. *The Lancet Infectious Diseases* **21**, e303–e317 (2021). [https://doi.org/10.1016/S1473-3099\(20\)30728-3](https://doi.org/10.1016/S1473-3099(20)30728-3).
- 506 [4] Assefa, D. G. *et al.* Efficacy and safety of different regimens in the treatment of patients with latent
507 tuberculosis infection: A systematic review and network meta-analysis of randomized controlled trials.
508 *Archives of Public Health* **81**, 82 (2023). <https://doi.org/10.1186/s13690-023-01098-z>.
- 509 [5] Li, T.-L. *et al.* Acquired Resistance to Isoniazid During Isoniazid Monotherapy in a Subject with Latent
510 Infection Following Household Rifampicin-Resistant Tuberculosis Contact: A Case Report. *Infect Drug Resist* **14**, 1505–1509 (2021). <https://doi.org/10.2147/IDR.S304799>.
- 512 [6] Dartois, V. A. & Rubin, E. J. Anti-tuberculosis treatment strategies and drug development: Challenges
513 and priorities. *Nat Rev Microbiol* **20**, 685–701 (2022). <https://doi.org/10/gqbtrn>.
- 514 [7] Vandal, O. H., Pierini, L. M., Schnappinger, D., Nathan, C. F. & Ehrt, S. A membrane protein preserves
515 intrabacterial pH in intraphagosomal Mycobacterium tuberculosis. *Nat Med* **14**, 849–854 (2008). <https://doi.org/10/drbt2b>.
- 517 [8] Goodsmith, N. *et al.* Disruption of an *M. tuberculosis* Membrane Protein Causes a Magnesium-dependent
518 Cell Division Defect and Failure to Persist in Mice. *PLOS Pathogens* **11**, e1004645 (2015). <https://doi.org/10/f67pgq>.
- 520 [9] Wang, R. *et al.* Persistent *Mycobacterium tuberculosis* infection in mice requires PerM for successful cell
521 division. *eLife* **8**, e49570 (2019). <https://doi.org/10.7554/eLife.49570>.

- 522 [10] Meade, R. K. *et al.* Genome-wide screen identifies host loci that modulate *Mycobacterium tuberculosis*
523 fitness in immunodivergent mice. *G3 Genes|Genomes|Genetics* **13**, jkad147 (2023). <https://doi.org/10/gtm6dn>.
- 525 [11] Paulussen, F. M. *et al.* Covalent Proteomimetic Inhibitor of the Bacterial FtsQB Divisome Complex.
526 *Journal of the American Chemical Society* **144**, 15303–15313 (2022). <https://doi.org/10/gtm6dp>.
- 527 [12] Wu, K. J. *et al.* Characterization of Conserved and Novel Septal Factors in *Mycobacterium smegmatis*. *J
528 Bacteriol* **200**, e00649–17 (2018). <https://doi.org/10/gtm6dr>.
- 529 [13] Gräve, K., Bennett, M. D. & Högbom, M. High-throughput strategy for identification of *Mycobacterium
530 tuberculosis* membrane protein expression conditions using folding reporter GFP. *Protein Expr Purif* **198**,
531 106132 (2022). <https://doi.org/10.1016/j.pep.2022.106132>.
- 532 [14] Korepanova, A. *et al.* Cloning and expression of multiple integral membrane proteins from *Mycobacterium
533 tuberculosis* in *Escherichia coli*. *Protein Sci* **14**, 148–158 (2005). <https://doi.org/2023101017072700228>.
- 534 [15] Baek, M. *et al.* Accurate prediction of protein structures and interactions using a three-track neural
535 network. *Science* **373**, 871–876 (2021). <https://doi.org/10/gk7nhq>.
- 536 [16] Evans, R. *et al.* Protein complex prediction with AlphaFold-Multimer. bioRxiv 2021.10.04.463034 (2022).
537 <https://doi.org/10.1101/2021.10.04.463034>.
- 538 [17] Attaibi, M. & den Blaauwen, T. An Updated Model of the Divisome: Regulation of the Septal Peptido-
539 glycan Synthesis Machinery by the Divisome. *Int J Mol Sci* **23**, 3537 (2022). <https://doi.org/10.3390/ijms23073537>.
- 541 [18] Craven, S. J., Condon, S. G. F. & Senes, A. A model of the interactions between the FtsQLB and
542 the FtsWI peptidoglycan synthase complex in bacterial cell division. bioRxiv 2022.10.30.514410 (2022).
543 <https://doi.org/10.1101/2022.10.30.514410>.
- 544 [19] Käshammer, L. *et al.* Cryo-EM structure of the bacterial divisome core complex and antibiotic target
545 FtsWIQBL. *Nat Microbiol* 1–11 (2023). <https://doi.org/10/gtm6dm>.
- 546 [20] Britton, B. M. *et al.* Conformational changes in the essential *E. coli* septal cell wall synthesis complex
547 suggest an activation mechanism. *Nat Commun* **14**, 4585 (2023). <https://doi.org/10/gtm4j5>.
- 548 [21] Park, K.-T., Park, D. J., Pichoff, S., Du, S. & Lutkenhaus, J. The essential domain of FtsN triggers
549 cell division by promoting interaction between FtsL and FtsI. bioRxiv 2023.05.12.540521 (2023). <https://doi.org/10/mmwf>.
- 551 [22] Bryant, P., Pozzati, G. & Elofsson, A. Improved prediction of protein-protein interactions using
552 AlphaFold2. *Nat Commun* **13**, 1265 (2022). <https://doi.org/10.1038/s41467-022-28865-w>.
- 553 [23] Varadi, M. *et al.* AlphaFold Protein Structure Database: Massively expanding the structural coverage
554 of protein-sequence space with high-accuracy models. *Nucleic Acids Research* **50**, D439–D444 (2022).
555 <https://doi.org/10.1093/nar/gkab1061>.
- 556 [24] Shaner, N. C. *et al.* A bright monomeric green fluorescent protein derived from *Branchiostoma lanceolatum*.
557 *Nat Methods* **10**, 407–409 (2013). <https://doi.org/10/f24459>.
- 558 [25] Goedhart, J. *et al.* Structure-guided evolution of cyan fluorescent proteins towards a quantum yield of
559 93%. *Nat Commun* **3**, 751 (2012). <https://doi.org/10.1038/ncomms1738>.
- 560 [26] Lee, P. A., Tullman-Ercek, D. & Georgiou, G. The Bacterial Twin-Arginine Translocation Pathway. *Annu
561 Rev Microbiol* **60**, 373–395 (2006). <https://doi.org/10.1146/annurev.micro.60.080805.142212>.
- 562 [27] Kiefer, D., Hu, X., Dalbey, R. & Kuhn, A. Negatively charged amino acid residues play an active role
563 in orienting the Sec-independent Pf3 coat protein in the *Escherichia coli* inner membrane. *The EMBO*

- 564 *Journal* **16**, 2197–2204 (1997). <https://doi.org/10.1093/emboj/16.9.2197>.
- 565 [28] Lucena, D., Mauri, M., Schmidt, F., Eckhardt, B. & Graumann, P. L. Microdomain formation is a general
566 property of bacterial membrane proteins and induces heterogeneity of diffusion patterns. *BMC Biol* **16**,
567 97 (2018). <https://doi.org/10.1186/s12915-018-0561-0>.
- 568 [29] Heckert, A., Dahal, L., Tjian, R. & Darzacq, X. Recovering mixtures of fast-diffusing states from short
569 single-particle trajectories. *eLife* **11**, e70169 (2022). <https://doi.org/10.7554/eLife.70169>.
- 570 [30] Hansen, A. S. *et al.* Robust model-based analysis of single-particle tracking experiments with Spot-On.
571 *eLife* **7**, e33125 (2018). <https://doi.org/10.7554/eLife.33125>.
- 572 [31] Wang, R. & Ehrt, S. Rv0954 Is a Member of the Mycobacterial Cell Division Complex. *Frontiers in
573 Microbiology* **12** (2021). <https://doi.org/10/gm8vsc>.
- 574 [32] Baranowski, C., Rego, E. H. & Rubin, E. J. The Dream of a Mycobacterium. *Microbiology Spectrum* **7**,
575 10.1128/microbiolspec.gpp3-0008-2018 (2019). <https://doi.org/10/gtm6dj>.
- 576 [33] Shlosman, I. *et al.* Allosteric activation of cell wall synthesis during bacterial growth. *Nat Commun* **14**,
577 3439 (2023). <https://doi.org/10.1038/s41467-023-39037-9>.
- 578 [34] Mirdita, M. *et al.* ColabFold: Making protein folding accessible to all. *Nat Methods* **19**, 679–682 (2022).
579 <https://doi.org/10.1038/s41592-022-01488-1>.
- 580 [35] Steinegger, M. & Söding, J. MMseqs2 enables sensitive protein sequence searching for the analysis of
581 massive data sets. *Nat Biotechnol* **35**, 1026–1028 (2017). <https://doi.org/10/ggctnw>.
- 582 [36] DeLano, W. L. Pymol: An open-source molecular graphics tool. *CCP4 Newsletter on protein
583 crystallography* **40**, 82–92 (2002).
- 584 [37] Sievers, F. *et al.* Fast, scalable generation of high-quality protein multiple sequence alignments using
585 Clustal Omega. *Mol Syst Biol* **7**, 539 (2011). <https://doi.org/10/bmv826>.
- 586 [38] Kunzmann, P. & Hamacher, K. Biotite: A unifying open source computational biology framework in
587 Python. *BMC Bioinformatics* **19**, 346 (2018). <https://doi.org/10.1186/s12859-018-2367-z>.
- 588 [39] Hallgren, J. *et al.* DeepTMHMM predicts alpha and beta transmembrane proteins using deep neural
589 networks. bioRxiv 2022.04.08.487609 (2022). <https://doi.org/10.1101/2022.04.08.487609>.
- 590 [40] Tareen, A. & Kinney, J. B. Logomaker: Beautiful sequence logos in Python. *Bioinformatics* **36**, 2272–2274
591 (2020). <https://doi.org/10.1093/bioinformatics/btz921>.
- 592 [41] Wu, E. L. *et al.* CHARMM-GUI Membrane Builder toward realistic biological membrane simulations.
593 *Journal of Computational Chemistry* **35**, 1997–2004 (2014). <https://doi.org/10/f6kgzz>.
- 594 [42] Huang, J. *et al.* CHARMM36m: An improved force field for folded and intrinsically disordered proteins.
595 *Nat Methods* **14**, 71–73 (2017). <https://doi.org/10/gfxkj3>.
- 596 [43] Eastman, P. *et al.* OpenMM 7: Rapid development of high performance algorithms for molecular dynamics.
597 *PLOS Computational Biology* **13**, e1005659 (2017). <https://doi.org/10/gbppkv>.
- 598 [44] Brown, T., Chavent, M. & Im, W. Molecular Modeling and Simulation of the Mycobacterial Cell Envelope:
599 From Individual Components to Cell Envelope Assemblies. *J. Phys. Chem. B* **127**, 10941–10949 (2023).
600 <https://doi.org/10.1021/acs.jpcb.3c06136>.
- 601 [45] Suh, D. *et al.* CHARMM-GUI Enhanced Sampler for various collective variables and enhanced sampling
602 methods. *Protein Sci* **31**, e4446 (2022). <https://doi.org/10.1002/pro.4446>.

- 603 [46] Miao, Y., Nichols, S. E., Gasper, P. M., Metzger, V. T. & McCammon, J. A. Activation and dynamic
604 network of the M2 muscarinic receptor. *Proceedings of the National Academy of Sciences* **110**, 10982–10987
605 (2013). <https://doi.org/10.1073/pnas.1309755110>.
- 606 [47] Gao, Y. *et al.* CHARMM-GUI Supports Hydrogen Mass Repartitioning and Different Protonation States
607 of Phosphates in Lipopolysaccharides. *Journal of Chemical Information and Modeling* **61**, 831–839 (2021).
608 <https://doi.org/10.1021/acs.jcim.0c01360>.
- 609 [48] Gowers, R. J. *et al.* MDAnalysis: A Python Package for the Rapid Analysis of Molecular Dynamics
610 Simulations. *Proceedings of the 15th Python in Science Conference* 98–105 (2016). <https://doi.org/10.25080/Majora-629e541a-00e>.
- 611 [49] Michaud-Agrawal, N., Denning, E. J., Woolf, T. B. & Beckstein, O. MDAnalysis: A toolkit for the analysis
612 of molecular dynamics simulations. *J Comput Chem* **32**, 2319–2327 (2011). <https://doi.org/10.1002/jcc.21787>.
- 613 [50] Zhang, M. *et al.* Rational design of true monomeric and bright photoactivatable fluorescent proteins. *Nat Methods* **9**, 727–729 (2012). <https://doi.org/10.1038/nmeth.2021>.
- 614 [51] Hensel, Z. A plasmid-based Escherichia coli gene expression system with cell-to-cell variation below the
615 extrinsic noise limit. *PLOS ONE* **12**, e0187259 (2017). <https://doi.org/10/gcg8pf>.
- 616 [52] Silva, J. P. N., Lopes, S. V., Grilo, D. J. & Hensel, Z. Plasmids for Independently Tunable, Low-Noise
617 Expression of Two Genes. *mSphere* **4** (2019). <https://doi.org/10/gf3vhf>.
- 618 [53] Neidhardt, F. C., Bloch, P. L. & Smith, D. F. Culture Medium for Enterobacteria. *J Bacteriol* **119**,
619 736–747 (1974).
- 620 [54] Schindelin, J. *et al.* Fiji: An open-source platform for biological-image analysis. *Nature methods* **9**, 676–82
621 (2012). <https://doi.org/10/f34d7c>.
- 622 [55] Cutler, K. J. *et al.* Omnipose: A high-precision morphology-independent solution for bacterial cell
623 segmentation. *Nat Methods* **19**, 1438–1448 (2022). <https://doi.org/10.1038/s41592-022-01639-4>.
- 624 [56] Sanial, M. *et al.* Direct observation of fluorescent proteins in gels: A rapid cost-efficient, and quantitative
625 alternative to immunoblotting. *bioRxiv* 2024.05.31.594679 (2024). <https://doi.org/10.1101/2024.05.31.594679>.
- 626 [57] Tinevez, J.-Y. *et al.* TrackMate: An open and extensible platform for single-particle tracking. *Methods*
627 **115**, 80–90 (2017). <https://doi.org/10.1016/j.ymeth.2016.09.016>.

632 Supplementary Figures

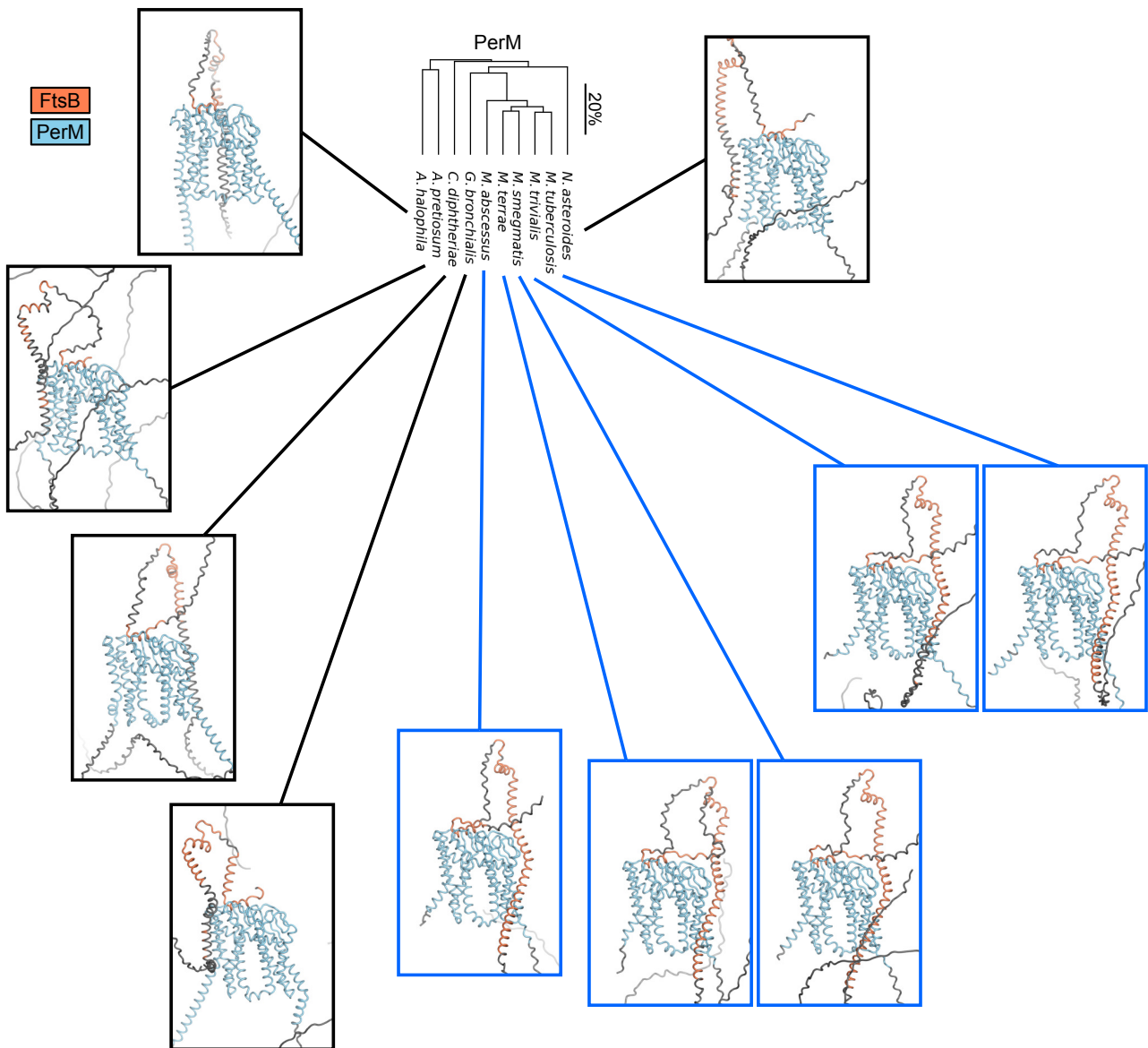


Fig. S1 The PerM phylogenetic tree from Fig. 1 is reproduced and compared to PerM-FtsB complexes predicted from full-length sequences for the same species. The predicted orientation of FtsBTM relative to PerM observed for Mtb is only observed for more closely related species (blue lines). However, FtsB^H interaction with PerM is predicted for all species. Residues with $pLDDT < 50$ are colored gray.

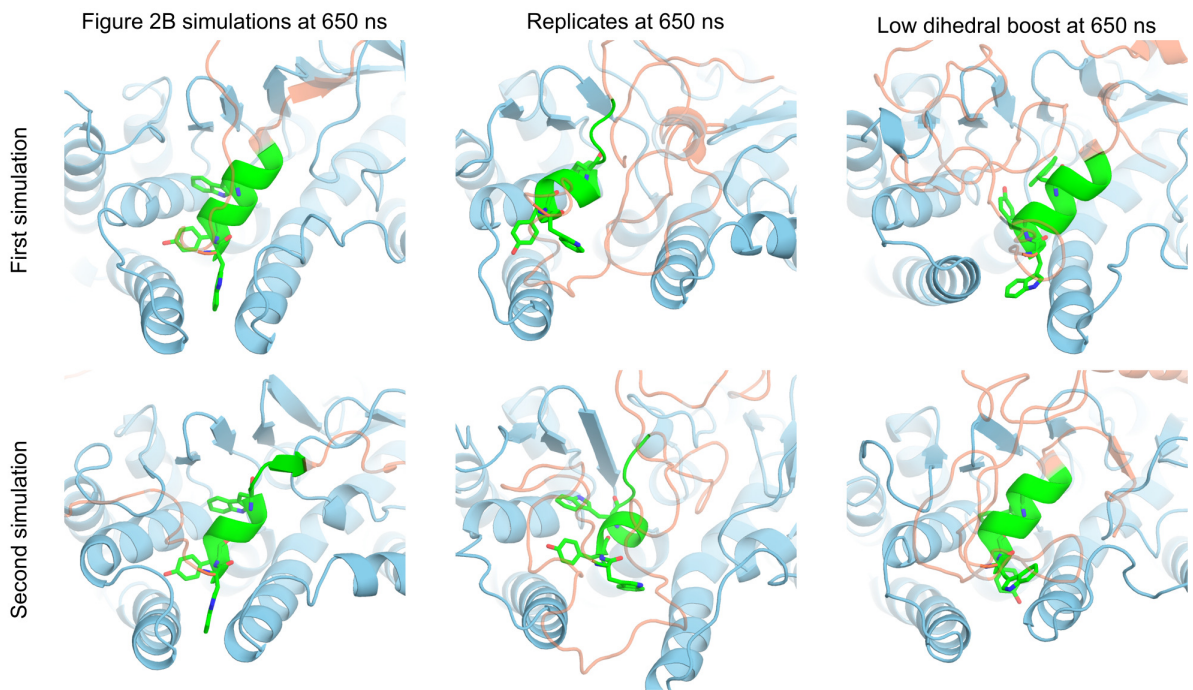
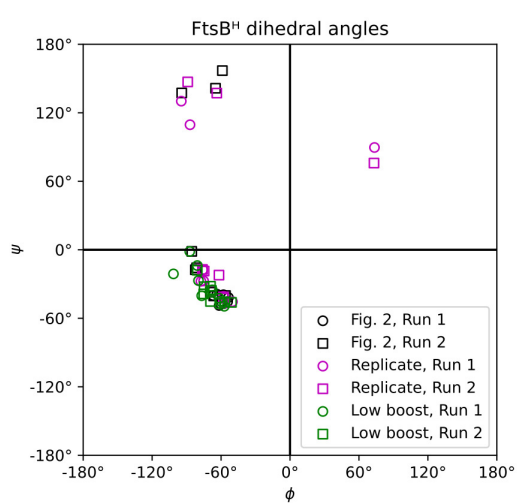
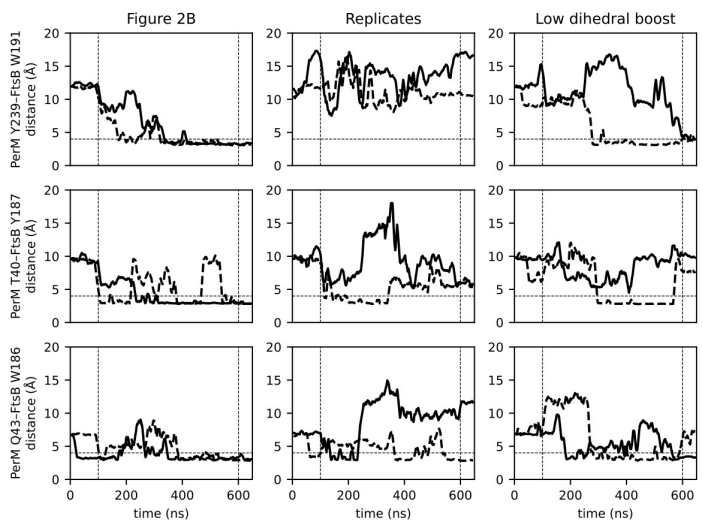
A**B****C**

Fig. S2 (A) Left: conformers at 650 ns for the PerM-FtsB aMD simulations described in the main text; FtsB^H residues are shown in green with a licorice representation for residues W186, Y187, and W191. Other FtsB residues are transparent orange and PerM is blue. FtsB^H secondary structure is disrupted in the second simulation. Middle: final conformers in two additional 650 ns replicate simulations. FtsB^H secondary structure is disrupted in both simulations. Right: final conformers in two 650 ns simulations in which λ value used to define dihedral boost parameters is reduced from 0.3 to 0.15. FtsB^H secondary structure is maintained in both simulations. (B) Ramachandran plot for FtsB^H residues in 650 ns conformers shows that α -helical dihedral angles are maintained for the first simulation in Fig. 2 and for both low boost simulations, but lost for residues in other simulations. (C) Left: reproduction of Fig. 2B plotted through 650 ns; a horizontal line is added at 4 Å. Middle: In replicate simulations that lose FtsB^H α -helical secondary structure, hydrogen bonds identified at the PerM-FtsB interface rarely form and a bond never forms between PerM Y239 and FtsB W191. Right: These hydrogen bonds form more frequently when the dihedral boost is reduced.

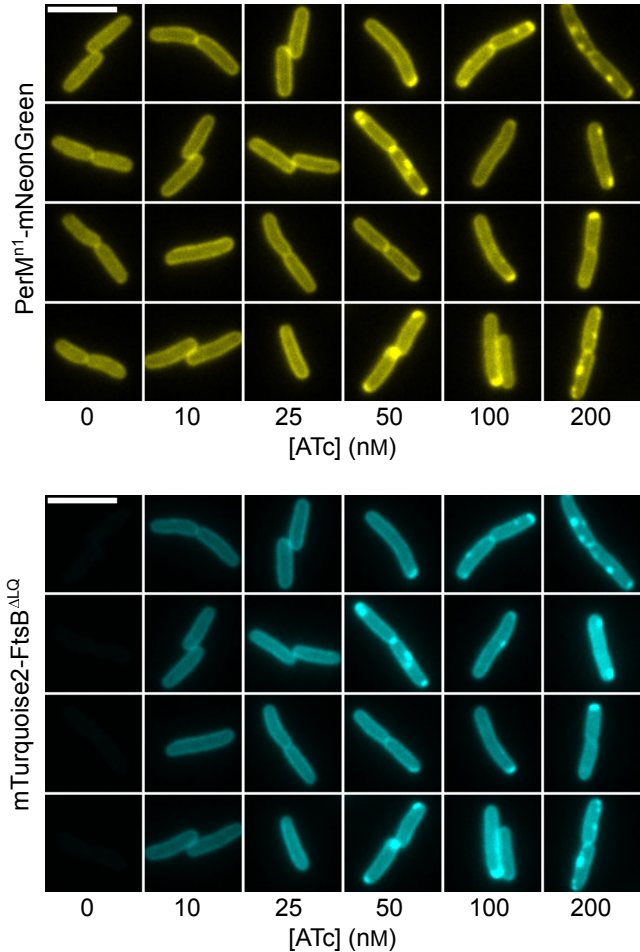


Fig. S3 ATc does not add substantial background to either mTurquoise2 or mNeonGreen images. Cells with plasmids expressing PerMⁿ¹-mNeonGreen and mTurquoise2-FtsB^{ΔLQ} were grown in the same conditions used for experiments reported in the main text with 100 μ M IPTG and with ATc at concentrations up to 20 \times the maximum concentration used in analyzed data. All images for each channel are shown with the same minimum and maximum intensity scaling to facilitate comparison of background and cellular fluorescence intensity. ATc concentrations at and above 50 nM (5 \times the concentration used in our experiments) led to aggregation and a lack of further mTurquoise2 fluorescence increase outside of aggregates; aggregation of PerMⁿ¹-mNeonGreen as well suggests that membrane protein translocation is beyond capacity for this strain and growth condition. No increase in background was observed in either channel at high ATc concentrations. Four regions of interest are shown for each condition with the same regions shown for both mNeonGreen and mTurquoise2 images.

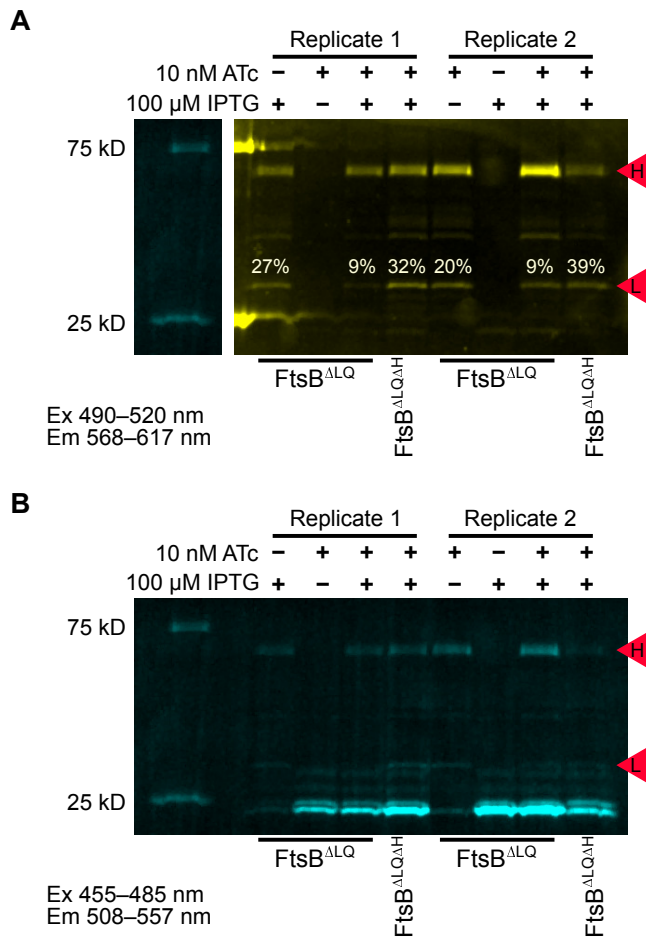


Fig. S4 Direct observation of PerMⁿ¹-mNeonGreen degradation by fluorescent SDS-PAGE. **(A)** Cell extracts for strains that all include a plasmid expressing PerMⁿ¹-mNG as well as mTq2-FtsB constructs with deletions corresponding to labels for each lane were grown in different induction conditions and separated by SDS-PAGE in conditions that maintain mNeonGreen and mTurquoise2 fluorescence. Degradation of PerMⁿ¹-mNG was quantified in two replicates of cell extracts as the integrated band intensity of the major degradation product (labeled L) relative to the sum of intensities for band L and band H, which has a molecular weight approximately corresponding to that of PerMⁿ¹-mNG (71 kD). Intermediate degradation products were not quantified. A weak band with lower molecular weight also appears in the absence of IPTG, and corresponds to a protein with mTurquoise2 fluorescence that is inefficiently detected in this channel. The ladder band is replaced with that from the blue/green image below because its fluorescence signal was extremely high for this yellow/red filter set; intermediate bands in this ladder are not strongly fluorescent in either channel. Although both bright fluorescent bands give background in adjacent lanes, this did not significantly impact measuring the intensity of either PerMⁿ¹-mNG band of interest. **(B)** The same gel as above was imaged with a blue/green filter set; in these extraction conditions used to quantify PerMⁿ¹-mNG degradation, full-length mTq2-FtsB constructs are not solubilized; instead, degradation products with mTurquoise2 fluorescence are observed near the expected 27 kD molecular weight of mTurquoise2.